

Spectroscopic Studies of Very Metal-Poor Stars with the Subaru High Dispersion Spectrograph. III. Light Neutron-Capture Elements¹

Wako Aoki², Satoshi Honda², Timothy C. Beers³, Toshitaka Kajino², Hiroyasu Ando², John E. Norris⁴, Sean G. Ryan⁵, Hideyuki Izumiura⁶, Kozo Sadakane⁷, Masahide Takada-Hidai⁸

ABSTRACT

Elemental abundance measurements have been obtained for a sample of 18 very metal-poor stars using spectra obtained with the Subaru Telescope High Dispersion Spectrograph. Seventeen stars, among which 16 are newly analyzed in the present work, were selected from candidate metal-poor stars identified in the HK survey of Beers and colleagues. The metallicity range covered by our sample is $-3.1 \lesssim [\text{Fe}/\text{H}] \lesssim -2.4$. The abundances of carbon, α -elements, and iron-peak elements determined for these stars confirm the trends found by previous work. One exception is the large over-abundance of Mg, Al and Sc found in BS 16934-002, a giant with $[\text{Fe}/\text{H}] = -2.8$. Interestingly, this is the most metal-rich star (by about 1 dex in $[\text{Fe}/\text{H}]$) known with such large overabundances in these elements. Furthermore, BS 16934-002 does *not* share the large over-abundances of carbon that are associated with the two other, otherwise similar, extremely metal-poor stars CS 22949-037 and CS 29498-043.

By combining our new results with those of previous studies, we investigate the distribution of neutron-capture elements in very metal-poor stars, focusing on the production of the light neutron-capture elements (e.g., Sr, Y, and Zr). Large scatter is found in the abundance ratios between the light and heavy neutron-capture elements (e.g., Sr/Ba, Y/Eu) for stars with low abundances of heavy neutron-capture elements.

²National Astronomical Observatory, Mitaka, Tokyo, 181-8588, Japan; email: aoki.wako@nao.ac.jp, honda@optik.mtk.nao.ac.jp, kajino@th.nao.ac.jp, ando@optik.mtk.nao.ac.jp

³Department of Physics and Astronomy, Michigan State University, East Lansing, MI 48824-1116; email: beers@pa.msu.edu

⁴Research School of Astronomy and Astrophysics, The Australian National University, Mount Stromlo Observatory, Cotter Road, Weston, ACT 2611, Australia; email: jen@mso.anu.edu.au

⁵Department of Physics and Astronomy, The Open University, Walton Hall, Milton Keynes, MK7 6AA, UK; email: s.g.ryan@open.ac.uk

⁶Okayama Astrophysical Observatory, National Astronomical Observatory, Kamogata-cho, Okayama, 719-0232, Japan; email: izumiura@oao.nao.ac.jp

⁷Astronomical Institute, Osaka Kyoiku University, Kashiwara, Osaka, 582-8582, Japan; email: sadakane@cc.osaka-kyoiku.ac.jp

⁸Liberal Arts Education Center, Tokai University, Hiratsuka, Kanagawa, 259-1292, Japan; email: hidai@apus.rh.u-tokai.ac.jp

Most of these stars have extremely low metallicity ($[\text{Fe}/\text{H}] \lesssim -3$). By contrast, the observed scatter in these ratios is much smaller in stars with excesses of heavy neutron-capture elements, and with higher metallicity. These results can be naturally explained by assuming that two processes independently enriched the neutron-capture elements in the early Galaxy. One process increases both light and heavy neutron-capture elements, and affects stars with $[\text{Fe}/\text{H}] \gtrsim -3$, while the other process contributes only to the light neutron-capture elements, and affects most stars with $[\text{Fe}/\text{H}] \gtrsim -3.5$. Interestingly, the Y/Zr ratio is similar in stars with high and low abundances of heavy neutron-capture elements. These results provide constraints on modeling of neutron-capture processes, in particular those responsible for the nucleosynthesis of light neutron-capture elements at very low metallicity.

Subject headings: nuclear reactions, nucleosynthesis, abundances — stars: abundances — stars: Population II

1. Introduction

Very metal-poor stars (hereafter, VMP stars, with $[\text{Fe}/\text{H}] \leq -2.0$)² belonging to the halo population of the Galaxy are believed to have formed at the earliest epoch of star formation, and preserve at their surfaces the chemical composition produced by the first generations of stars. Studies of the chemical composition of VMP stars have, in the past decade, proven to be very important for understanding individual nucleosynthesis processes (e.g., McWilliam et al. 1995; Ryan, Norris, & Beers 1996; Cayrel et al. 2004). In particular, the abundances of the neutron-capture elements provide strong constraints on the modeling of explosive nucleosynthesis, and for identifying the likely astrophysical sites in which they are produced.

One surprising result found by previous studies is the existence of a large scatter in measured abundance ratios between the neutron-capture elements and other metals (e.g., Ba/Fe). The scatter appears most significant at $[\text{Fe}/\text{H}] \sim -3$. For instance, the abundance ratio of [Ba/Fe] in stars near this metallicity exhibits a range of about three dex (e.g., McWilliam 1998). Some of the Ba-enhanced stars have abundance patterns that can be explained by the slow neutron-capture process (s-process). These stars typically also have high abundances of carbon. Such carbon-enhanced, metal-poor, s-process-rich (hereafter, CEMP-s) stars are believed to belong to binary systems, the presently observed member having been polluted by an Asymptotic Giant Branch (AGB) companion through mass transfer at an earlier epoch. However, even after removing the

¹Based on data collected at the Subaru Telescope, which is operated by the National Astronomical Observatory of Japan.

² $[\text{A}/\text{B}] = \log(N_{\text{A}}/N_{\text{B}}) - \log(N_{\text{A}}/N_{\text{B}})_{\odot}$, and $\log \epsilon_{\text{A}} = \log(N_{\text{A}}/N_{\text{H}}) + 12$ for elements A and B.

CEMP-s stars from samples of objects with metallicity near $[\text{Fe}/\text{H}] = -3.0$, a large scatter in $[\text{Ba}/\text{Fe}]$ remains.

Even though the abundance ratios between neutron-capture elements and lighter metals like iron exhibit significant scatter, the abundance patterns of heavy neutron-capture elements (Ba–Os) in stars with $[\text{Fe}/\text{H}] < -2.5$ agree very well with that of the r-process component in solar system material (e.g., Sneden et al. 1996; Westin et al. 2000; Cayrel et al. 2001). This fact indicates that the neutron-capture elements in metal-poor, non CEMP-s stars have originated from the r-process. From the abundance ratios of Ba/Eu or La/Eu, Burris et al. (2000) and Simmerer et al. (2004) concluded that significant contributions from the (main) s-process appear at $[\text{Fe}/\text{H}] \sim -2.3$, though small effect of the s-process is also suggested at slightly lower $[\text{Fe}/\text{H}]$ (~ -2.7).

The large scatter in $[\text{Ba}/\text{Fe}]$ in stars with $[\text{Fe}/\text{H}] < -2.5$ means that the astrophysical site responsible for this process was different from the site responsible for Fe production, and the elements produced were not well mixed into the interstellar matter from which the low-mass stars we are currently observing were formed. Moreover, the above observational result suggests that the abundance pattern of the solar-system r-process component is not the result of a mixture of yields from individual nucleosynthesis events having very different abundance patterns, but rather is a result of nucleosynthesis processes that yielded very similar abundance patterns for these elements throughout Galactic history. This phenomenon is sometimes referred to as the “universality” of the r-process nucleosynthesis, and it is believed to be a key for understanding this process, as well as for the use of the heaviest radioactive nuclei (Th and U) as cosmo-chronometers to place direct limits on the ages of extremely metal-poor (EMP; $[\text{Fe}/\text{H}] \lesssim -3.0$) and VMP stars.

By way of contrast, measured abundance ratios between *light* neutron-capture elements, such as Sr ($Z = 38$), and *heavy* ones ($Z \geq 56$) in VMP stars exhibit a large dispersion (e.g., McWilliam 1998). The abundance patterns from Sr to Ba in stars with enhancements of r-process elements do *not* agree well with that of the solar-system r-process component (Sneden et al. 2000). In other words, the universality of the r-process apparently does not apply to the lighter neutron-capture elements.

The processes responsible for the synthesis of light neutron-capture elements have been recently studied with growing interest. Truran et al. (2002) pointed out the existence of a group of stars that exhibit high Sr/Ba ratios but low Ba abundances, and emphasized the contrast to r-process-enhanced stars that have relatively low Sr/Ba ratios. These authors suggested the existence of a quite different origin of these elements than those (heavier) elements formed by the “main” r-process. Travaglio et al. (2004) investigated the production of light neutron-capture elements, Sr, Y, and Zr, from the point of view of Galactic chemical evolution. They concluded that there must exist a process that has provided these light neutron-capture elements throughout Galactic history, which they referred to as the “lighter element primary process (LEPP)”, and estimated its contribution to the abundances of Sr, Y, and Zr in solar-system material.

Thus, although the existence of a process that produces light neutron-capture elements without

significant contribution to the heavier ones is suggested by several previous studies, its astrophysical site remains unclear. This process is usually distinguished from the weak s-process, which is believed to occur in helium-burning massive stars, but thought to be inefficient at low metallicity. It is clearly desirable to obtain additional observational constraints on the nature of this unknown process for the production of light neutron-capture elements, such as the elemental abundance patterns produced by the process, and the level of its contribution to stars with different metallicity. Although some observational studies (e.g., Johnson & Bolte 2002) have previously focused on this issue, and have provided important abundance results, more studies for larger sample of stars with very low metallicity and accurately measured abundances are required.

Our previous study determined chemical abundances for 22 VMP stars, and discussed the abundance ratios of neutron-capture elements (Honda et al. 2004a, b: hereafter, Paper I and Paper II, respectively). In Paper II, we investigated the correlation between Sr and Ba abundances for stars with $[\text{Fe}/\text{H}] < -2.5$, and found that the scatter of the Sr abundance ($\log \epsilon(\text{Sr})$) increases with decreasing Ba abundance. The present paper reports the chemical abundances for an additional 16 VMP stars, as well as for two stars that have already been studied in Paper II, based on observations obtained with the Subaru Telescope High Dispersion Spectrograph (HDS; Noguchi et al. 2002) during its commissioning phase.

In Section 2, we describe the sample selection, details of the observations, and measurements of equivalent widths and radial velocities. Elemental abundance measurements are presented in Section 3. In this section we also consider a new star that exhibits a significantly high Mg/Fe abundance ratio compared to other VMP stars in our study. In Section 4 we combine the chemical abundances for VMP stars reported by previous work with our new sample, and discuss the production of light neutron-capture elements in the early Galaxy.

2. Observations and Measurements

2.1. Sample Selection and Photometry Data

Our sample of stars was originally selected from candidate very metal-poor stars identified in the HK survey of Beers and colleagues (Beers, Preston, & Shectman 1985; 1992; Beers 1999) whose medium-resolution (1–2 Å) spectra indicated that they possessed metallicities $[\text{Fe}/\text{H}] \leq -2.5$. While in Paper II we selected objects that were likely to have excesses of r-process elements, our new sample has no such explicit bias. Indeed, none of the objects in the new sample exhibit significant excesses of heavy neutron-capture elements (see below). Nevertheless, the abundances of light neutron-capture elements such as Sr are distributed over a very wide range in our new sample. Table 1 provides a listing of the objects considered in our study, including their coordinates, details of the observations conducted, and their measured radial velocities (see below).

The neutron-capture element-enhanced star CS 30306–132 was already analyzed in Paper II,

but is also included here for comparison purposes. For the same reason, the bright metal-poor giant HD 122563 was also analyzed.

Table 2 presents optical *BVRI* photometry (Johnson–Kron–Cousins system) for our sample stars; with the exception of HD 122563, these data are drawn from photometry reported by Beers et al. (2005, in preparation). Errors in the *BVRI* magnitudes are typically on the order of 0.01–0.02 magnitudes. Near infrared *JHK* photometry was, again with the exception of HD 122563, provided by the Two Micron All Sky Survey (2MASS) Point Source Catalog (Skrutskie et al. 1997). Estimates of the interstellar reddening, $E(B - V)$, for each object were obtained from the Schlegel, Finkbeiner, & Davis (1998) map; the extinction of each band was obtained from the reddening relation provided in their Table 6.

2.2. High-Dispersion Spectroscopy

High-dispersion spectroscopy for the purpose of conducting our chemical abundance studies was obtained with Subaru/HDS, using a spectral resolving power $R = 50,000$ (a slit width of 0.72 arcsec), in April 2001, July 2001, and February 2002. The atmospheric dispersion corrector (ADC) was used in all observing runs. Two EEV-CCDs were used with no on-chip binning. The spectra cover the wavelength range 3550–5250 Å, with a small gap in the coverage between 4350 and 4450 Å due to the physical separation between the two CCDs.

The object list and observing details are given in Table 1. Standard data reduction procedures (bias subtraction, flat-fielding, background subtraction, extraction, and wavelength calibration) were carried out with the IRAF echelle package³. In order to remove suspected cosmic-ray hits, we first apply median filtering to a two-dimensional CCD image. When a remarkably high count was found at one pixel in the original image compared to the median-filtered image, the recorded counts of that pixel were replaced by the value obtained in the median-filtered image.⁴ Wavelength calibration was performed using Th-Ar spectra obtained a few times during each night of

³IRAF is distributed by the National Optical Astronomy Observatories, which is operated by the Association of Universities for Research in Astronomy, Inc. under cooperative agreement with the National Science Foundation.

⁴At the beginning of the data reduction, we subtracted bias level from each object frame. Since the inter-order region of the object frame has very low count, we first added a constant to object frame, and then applied the IRAF task *median* to make median-filtered image (with the parameter $x[y]window$ of 3). The constant added to the object frame is the same order of the peak count due to the photons from the star. We divided the object frame by the median-filtered image, resulting in a frame which has count close to unity, with exceptions of pixels affected by cosmic-ray. We identified the pixels that have counts more than 20 % higher than those in surrounding pixels as those affected by cosmic-ray, and replaced their counts by unity (this process is more effectively made by applying the task *lineclean* to fitting to both column and line directions). We multiply the obtained frame by the median-filtered image, and finally subtract the constant that was added at the first process. We confirmed the above parameter choices are quite conservative, i.e., this procedure does not affect the pixels which are apparently not affected by cosmic-ray events, though there remain some pixels which seem to be affected by cosmic-ray.

observations.

The signal-to-noise (S/N) ratio given in Table 1 was estimated from the peak counts of the spectra in the 149th Echelle order ($\sim 4000 \text{ \AA}$). We note that the values are given per resolution element (6 km s^{-1}). Since the resolution element is covered by about 6.7 pixels, the S/N ratios per pixel are by a factor of ~ 2.6 lower than those listed in the table.

2.3. Equivalent Widths

Equivalent widths were measured for isolated atomic lines by fitting gaussian profiles (Press et al. 1996), while a spectrum synthesis technique was applied to CH molecular bands, as well as to atomic lines that are significantly affected by hyperfine splitting. The measured equivalent widths of elements lighter than La ($Z \leq 56$) are given in Table 3. Heavier elements are detected only in stars having relatively higher abundances of neutron-capture elements. The measured equivalent widths of heavier elements are given for 11 objects in Table 4 separately.

Comparisons of equivalent widths with those reported in Paper I are shown in Figure 1 for HD 122563 and CS 30306–132. While the same data were analyzed for CS 30306–132 in both studies, our data for HD 122563 are different than those in Paper I. Measurements of equivalent widths were made independently by W.A. (this work) and S.H. (Paper I) using different software, although both applied gaussian fitting procedures. The two measurements show quite good agreement, although small departures appear for the strongest lines; the trends are opposite for the two stars, suggesting these are not systematic in origin. Most likely, they are the result of adopting slightly different fitting ranges for strong lines by the two investigators.

Comparisons with the measurements by Cayrel et al. (2004) are also shown in Figure 2 for HD 122563 and CS 30325–094. The agreement is again quite good; there is no obvious systematic differences between the two sets of measurements.

The equivalent widths of the two resonance lines of Ba require special attention. Comparisons of the equivalent widths between the two lines are shown in Figure 3. The equivalent width of the Ba II 4934 \AA line is sometimes larger than that of the 4554 \AA line, even though the gf -value of the 4934 \AA is smaller, by a factor of two, than that of the 4554 \AA line. This apparent discrepancy is not necessarily due to measurement error. First, the wavelength of the former line is larger by $\sim 8\%$ than the latter one, and correction for this factor is required in order to compare the equivalent widths. In addition, the effect of hyperfine splitting is expected to be more significant for the 4934 \AA line than that for the 4554 \AA line, if isotopes with odd mass number (^{135}Ba and ^{137}Ba) significantly contribute to the absorption. We simulated these effects by calculating equivalent widths of both lines using a model atmosphere for a metal-poor giant, assuming Ba isotope fractions of the r-process component in solar-system material (Arlandini et al. 1999). The results are shown by the solid line in Figure 3. Our calculations demonstrate that, after the small correction for the difference of the wavelengths, the equivalent width of the 4554 \AA is twice that of the 4934 \AA line in the weak-line

limit ($W \lesssim 20 \text{ m}\text{\AA}$), but the equivalent widths of the two lines are similar at $W \sim 120 \text{ m}\text{\AA}$; the equivalent width of the 4934 \AA is larger than that of 4554 \AA if the lines are stronger. We also show the results of calculations not including hyperfine splitting for comparison purposes (the dashed line in the figure). The measured equivalent widths of strongest lines are better explained by the calculations taking account of the effect of hyperfine splitting. This suggests a large contribution from isotopes with odd mass numbers, which are expected as a result of r-process nucleosynthesis. This would be consistent with the fact that the objects having strong Ba lines in our sample show abundance ratios (e.g., Ba/Eu ratios) similar to that of the r-process component in solar system material (see below).

2.4. Radial velocities

We measured heliocentric radial velocities (V_r) for each spectrum, as given in Table 1. The measurements were made using clean, isolated Fe I lines. The standard deviation of the values from individual lines is adopted as the error of the measurements reported in the table. Systematic errors in the measurements are not included in these errors. The wavelength calibration was made using Th-Ar comparison spectra that were obtained during the observing runs, without changing the spectrograph setup. Hence, the systematic error is basically determined by the stability of the spectrograph. The spectrum shift during one night is at most 0.5 pixel (0.45 km s^{-1}), which corresponds to a temperature variation of four degrees centigrade (Noguchi et al. 2002), if the setup is not changed during the night. Combining this possible systematic error with the random errors (the 3σ level is typically $0.6\text{--}0.8 \text{ km s}^{-1}$), the uncertainties of the reported radial velocity measurements are $0.7 \sim 1.0 \text{ km s}^{-1}$.

For three stars in our sample (BS 16934–002, CS 30306–132, and CS 30325–028), two or three spectra were obtained on different observing runs. While no clear variation of V_r is found in BS 16934–002 and CS 30306–132, CS 30325–028 exhibits a 2.4 km s^{-1} difference between the two measurements, suggesting possible binarity of this object. Further monitoring of radial velocity for this object is required to determine its binary nature, which may be related to its chemical abundance properties.

The heliocentric radial velocity of HD 122563 measured in our study is $V_r = -25.81 \text{ km s}^{-1}$. This is similar to the previous measurements reported in Paper I and in Norris, Ryan, & Beers (1996) ($V_r = -26.5 \sim -27.2 \text{ km s}^{-1}$). A radial velocity $V_r = -108.46 \text{ km s}^{-1}$ was obtained for CS 30306–132 from the 2001 July spectrum. This agrees, within the errors, with the results obtained from the independent measurement reported in Paper I using the same spectra.⁵

⁵Note that the sign of the V_r of CS 30306–132 in Paper I is not correct: the correct value is $V_r = -109.01 \text{ km s}^{-1}$.

3. Chemical Abundance Analysis and Results

A standard analysis using model atmospheres was performed for the measured equivalent widths for most of the detectable elements, while a spectrum synthesis technique was applied for the CH molecular bands and atomic lines strongly affected by hyperfine splitting. For the calculation of synthetic spectra and equivalent widths using model atmospheres, we applied the LTE spectral synthesis code used in Aoki & Tsuji (1997). Unsöld (1955)’s treatment of van der Waals broadening, enhanced by a factor of 2.2 in γ , was used as in Ryan, Norris, & Beers (1996). The polynomial partition function approximations provided by Irwin (1981) were applied to the heavy elements. In this section we describe the determination of stellar atmospheric parameters (subsection 3.1) and abundance measurements for carbon (subsection 3.2), α -elements (subsection 3.3), and the neutron-capture elements (subsection 3.4) in detail. Estimates of uncertainties in abundance measurements are presented in subsection 3.5.

3.1. Atmospheric Parameters

Effective temperatures were estimated from the photometry listed in Table 2 using the empirical temperature scale of Alonso, Arribas, & Martínez-Roger (1999), after reddening corrections were carried out. The filter-corrections of Fernie (1983) were applied to convert the Johnson-Kron-Cousins $V - R$, $V - I$, and $R - I$ colors to Johnson ones that were used in the temperature scale of Alonso, Arribas, & Martínez-Roger (1999). The filter-corrections provided by Carpenter (2001) and Alonso, Arribas, & Martínez-Roger (1994) were applied to 2MASS J , H , and K data to derive those in the TSC system (via the CIT ones) that is used by Alonso, Arribas, & Martínez-Roger (1999). We have chosen to adopt the values determined from $V - K$, as described in Paper II (Table 2). For comparison purposes, we also give the difference between the effective temperature from the $V - K$ and the average of the effective temperature from four colors ($B - V$, $V - R$, $V - I$ and $R - I$). The agreement is quite good, less than ± 100 K, between the effective temperatures derived from $V - K$ and from the average of the optical bands.

The effective temperatures adopted in the abundance analyses are listed in Table 5. Note that the near infrared photometry data were not available for several objects when our first abundance analyses were made. In these cases, we estimated the effective temperature from the optical colors (e.g., $B - V$), and performed a re-analysis if the effective temperature obtained from $V - K$ is significantly different from that adopted in our first analyses. In other cases, we did not repeat the analysis. The largest difference of the effective temperature from $V - K$ and adopted one is 79 K (CS 30306–132), which is below the expected error of the effective temperature determination.

An LTE abundance analysis was carried out for Fe I and Fe II lines using the model atmospheres of Kurucz (1993). We performed abundance analyses in the standard manner for the measured equivalent widths. Surface gravities ($\log g$) were determined from the ionization balance between Fe I and Fe II; the microturbulent velocity (v_{turb}) was determined from the Fe I lines by demanding

no dependence of the derived abundance on equivalent widths. The final atmospheric parameters are reported in Table 5.

We note that there exists a correlation between the lower excitation potential (χ) of Fe I lines and the abundance derived from individual lines. The slope is typically $-0.04 \text{ dex eV}^{-1}$. Such correlations were already reported by Johnson (2002) who also applied the Kurucz’s model atmosphere grid to the analyses of very metal-poor giants. This trend disappears if systematically lower effective temperatures (by about 150 K) are assumed (Johnson 2002). Hence, our effective temperatures might be systematically higher than those determined spectroscopically in previous studies.

3.2. Carbon

Carbon abundances were estimated from the CH molecular band at 4322 Å following the procedures described in Paper II, using the same line list for the CH band. The band was detected in all stars except for CS 30327–038, for which only an upper limit of the carbon abundance could be estimated.

The carbon abundances of HD 122563 and CS 30306–132 were also determined by Paper II. The present work adopts similar atmospheric parameters to those in the previous one, and the agreement between the two measurements is fairly good.

The carbon abundances of HD 122563 and CS 30325–094 were also measured by Cayrel et al. (2004) from the G-band of the CH $A - X$ system. While the agreement of the $[C/Fe]$ values for HD 122563 between the two works is fairly good, the $[C/Fe]$ determined by our present analysis for CS 30325–094 is 0.5 dex higher than that of Cayrel et al. (2004). The discrepancy can be partially (~ 0.2 dex) explained by the small difference of the adopted effective temperatures (100 K). However, the reason for the remaining discrepancy is not clear.

The carbon abundances of giants are expected to be affected by internal processes, i.e., CNO-cycle and dredge-up. Figure 4 shows the correlation between the carbon abundance ratio ($[C/Fe]$) and luminosity ($\log L/L_{\odot}$) that is estimated using the relation $L/L_{\odot} \propto (R/R_{\odot})^2 (T_{\text{eff}}/T_{\text{eff}\odot})^4 \propto (M/M_{\odot})(g/g_{\odot})^{-1} (T_{\text{eff}}/T_{\text{eff}\odot})^4$, assuming the mass of the stars to be $0.8 M_{\odot}$, for our sample and those of Paper II and Cayrel et al. (2004). While the bulk of stars with $\log L/L_{\odot} \lesssim 2.5$ have $[C/Fe] \sim +0.4$, $[C/Fe]$ decreases with increasing luminosity.⁶ This decreasing trend can be interpreted as a result of internal processes. Similar tendency was already found by Cayrel et al. (2004) who investigated the correlation between $[C/Fe]$ and effective temperature for their sample. However, the trend is more clear in our figure where luminosity is adopted as the indicator of the evolutionary stage. A more detailed analysis for the Cayrel et al.’s sample was made by Spite et al.

⁶A few stars have exceptionally high carbon abundances ($[C/Fe] \sim +1.0$) at high luminosity ($\log L/L_{\odot} \sim 2.7$). The well known carbon-enhanced objects CS 22892–052 and CS 22949–037 are included in this group.

(2005), including N and Li abundances. A similar discussion is also found in Carretta, Gratton & Sneden (2000) for more metal-rich stars.

3.3. The α and Iron-Peak Elements

There are numerous previous studies of the α - and iron-peak elements in VMP stars. Our measurements confirm the usual over-abundances of α -elements relative to iron that have been found previously for the majority of metal-poor stars. Figure 5 shows the trend of $[\text{Mg}/\text{Fe}]$ as a function of $[\text{Fe}/\text{H}]$. A Mg over-abundance of about 0.4–0.6 dex is found for most stars in our sample. These values are similar to the majority of metal-poor dwarf stars reported by Cohen et al. (2004) and to the giants studied in Paper II. Note that these two studies found several stars with low abundances of α -elements ($[\text{Mg}/\text{Fe}] \sim 0.0$), while no such star is found in the present sample.

The $[\text{Mg}/\text{Fe}]$ values of giants studied by Cayrel et al. (2004) seem to be slightly (0.10–0.15 dex) lower than those of our stars. Since only two stars are in common between the two studies, this discrepancy may be simply due to differences in the samples under consideration. However, the $[\text{Mg}/\text{Fe}]$ of HD 122563 determined by us is +0.54, while Cayrel et al. (2004) derived $[\text{Mg}/\text{Fe}] = +0.36$ for the same object ($\Delta [\text{Mg}/\text{Fe}] = 0.18$ dex). Hence, there seems to exist a systematic difference between the two studies. We note that the $[\text{Mg}/\text{Fe}]$ of HD 122563 determined in Paper II ($[\text{Mg}/\text{Fe}] = +0.54$) agrees with our result.

Measurements of Mg/Fe ratios are relatively insensitive to the adopted atmospheric parameters (subsection 3.5). Hence, the difference of model parameters between our study and Cayrel et al. (2004) for metal-poor giants is not likely to be the source for the discrepancies in the derived $[\text{Mg}/\text{Fe}]$ values. However, it should be noted that the Mg lines used in the abundance measurements in these two studies are somewhat different. For instance, the present study uses the Mg I 4057.5 and 4703.0 Å lines, which were not adopted by Cayrel et al. (2004), while they used Mg I 4351.9 and 5528.405 Å lines that are not covered by our spectral range. Moreover, the gf -values of some lines are different (e.g., Mg I 4570 Å line: their $\log gf$ value is 0.3 dex higher than ours). These differences may partially explain the discrepancies in the Mg/Fe ratios. We attempted an analysis of Mg abundance for HD 122563 using the equivalent widths and line data of Cayrel et al. (2004), and derived $[\text{Mg}/\text{Fe}] = +0.45$. The discrepancy ($\Delta [\text{Mg}/\text{Fe}] = 0.09$ dex) then becomes much smaller than the original one. Nevertheless, there seems to remain a ~ 0.1 dex discrepancy in $[\text{Mg}/\text{Fe}]$ between the two studies for which no clear reason has been found.

We call attention to the very large Mg over-abundance in BS 16934–002 ($[\text{Mg}/\text{Fe}] = +1.25$). Figure 6 shows examples of Mg absorption features in this star, compared to those of HD 122563, which has similar atmospheric parameters and iron abundance. While the strengths of the Fe absorption lines are very similar in the two objects, the Mg absorption lines in BS 16934–002 are clearly much stronger than those in HD 122563. We note that the lower excitation potential of the two Mg lines shown in this figure are quite different, hence the stronger Mg absorption

features in BS 16934–002 is not due to the (small) differences of atmospheric parameters in the two stars. The derived Ti abundance of BS 16934–002 relative to Fe is slightly higher than other stars in our sample, including HD 122563. This is also seen in the spectra shown in Figure 6. Another remarkable abundance anomaly found in BS 16934–002, compared to other stars, is its high abundances of Al ($[Al/Fe]=+0.03$) and Sc ($[Sc/Fe]=+0.7$).

There are two other well-studied stars with $[Fe/H]=-3.5 \sim -4.0$ having extremely high Mg/Fe ratios (CS 22949–037: McWilliam et al. 1995, Norris et al. 2001, Depagne et al. 2002; CS 29498–043: Aoki et al. 2002a). These two stars also exhibit large over-abundances of C, N, O, and Si, hence they might be more properly interpreted as “iron-deficient” stars, perhaps related to supernovae that ejected only small amount of material from their deepest layers (Tsujiimoto & Shige-yama 2003; Umeda & Nomoto 2003). It is thus of some significance that BS 16934–002 has *no clear excess* of either C or Si. Its iron abundance is more than five times higher than the two stars. Hence, the origin of the Mg excess in BS 16934–002 is perhaps quite different from that in CS 22949–037 and CS 29498–043. Further chemical abundance measurements based on higher quality spectra are clearly needed to understand the nucleosynthesis processes responsible for this star. In particular, oxygen would be a key element to measure.

3.4. The Neutron-Capture Elements

The abundances of Sr and Ba were determined by a standard analysis of the Sr II and Ba II resonance lines. Because of their large transition probabilities and the relatively high abundances of these two elements in our stars, Sr and Ba are detected in all of our program objects. An exception is the Ba in CS 30325–094, for which only an upper limit of its abundance was determined. In the analyses of the Ba lines, the effects of hyperfine splitting and isotope shifts are included, assuming the isotope ratios of the r-process component of solar system material. The Ba in such VMP stars is expected to have originated from the r-process, except for stars with large excesses of carbon and s-process elements (e.g., McWilliam 1998). Since the metallicity range covered by our sample is $[Fe/H] \leq -2.4$, where contributions of the s-process is small in general (see Section 1), and no CEMP-s stars are included in our sample, the above assumption is quite reasonable for our analyses. The effect of hyperfine splitting is clearly seen in stars with strong Ba lines, as mentioned in subsection 2.3.

The light neutron-capture elements Y and Zr are detected in 14 and 11 stars in our sample, respectively. The derived abundances of these four elements (Sr, Y, Zr, and Ba) are listed in Table 6. An upper-limit of the abundance is given when no absorption line is detected.

Our sample includes no stars with significant over-abundances of heavy neutron-capture elements, with the exception of CS 30306–132, which was already studied in Paper II and is re-analyzed here for comparison purposes. For this reason, elements heavier than Ba are detected only in a limited number of objects. The abundances of these heavy elements are given in Table 7. The

abundances were determined by standard analysis techniques, taking into account hyperfine splitting for La (Lawler et al. 2001a) and Yb (Snedden 2003, private communication). For the element Eu a spectrum synthesis technique was applied because the three Eu II lines analyzed in the present work show remarkably strong effects of hyperfine splitting (Lawler et al. 2001b). An isotope ratio of $^{151}\text{Eu}:^{153}\text{Eu}=50:50$ was assumed in the analysis.

Figure 7 shows the abundance patterns of seven elements from Zn to Eu for BS 16543–097 and BS 16080–054, whose Zn abundances are quite similar. BS 16543–097 is a star having relatively high abundances of heavy neutron-capture elements as compared to most stars in our sample, while the abundances of these elements in BS 16080–054 are lower by about 1 dex than those in BS 16543–097. Nevertheless, the abundance patterns from Zn to Zr are very similar in the two stars. Such large difference in the abundance ratios between light and heavy neutron-capture elements has already been reported in a number of VMP stars (e.g., Truran et al. 2002), and suggests the existence of two (or more) processes that produce neutron-capture elements. This point is discussed in detail in Section 4.

3.5. Uncertainties

Random abundance errors in the analysis are estimated from the standard deviation of the abundances derived from individual lines for each species. These values are sometimes unrealistically small, however, when only a few lines are detected. For this reason, we adopted the larger of (a) the value for the listed species and (b) that for Fe I as estimates of the random errors. Typical random errors are on the order of 0.1 dex.

We estimated the upper limit of the chemical abundances for several elements when no absorption line is detected. The error of equivalent width measurements is estimated using the relation $\sigma_W \sim (\lambda n_{\text{pix}}^{1/2}) / (R[S/N])$, where R is the resolving power, S/N is the signal-to-noise ratio per pixel, and $n_{\text{pix}}^{1/2}$ is the number of pixels over which the integration is performed (Norris, Ryan, & Beers 2001). The upper limit of equivalent widths, used to estimate the upper limit of abundances, is assumed to be $3\sigma_W$.

Errors arising from uncertainties of the atmospheric parameters were evaluated for $\sigma(T_{\text{eff}}) = 100$ K, $\sigma(\log g) = 0.3$ dex, and $\sigma(v_{\text{tur}}) = 0.3$ km s $^{-1}$ for HD 122563, CS 30306–132, and CS 29516–041. HD 122563 is a well-known metal-poor giant. CS 30306–132 has high abundances of neutron-capture elements, while these elements in CS 29516–041 are relatively deficient. We applied the errors estimated for elements other than neutron-capture elements for HD 122563 to all other stars. The strengths of absorption lines of neutron-capture elements show a quite large scatter in our sample. Since the errors in abundance measurements are sensitive to the line strengths, we estimated errors in abundance measurements including the difference of line strengths as follows. (1) Light neutron-capture elements – we applied the errors for Sr, Y, and Zr estimated for HD 122563 to most stars. For stars with weak Sr lines, we adopted the errors estimated for CS 29516–041 (in

such objects, Y and Zr are not detected). (2) Heavy neutron-capture elements – we applied the errors estimated for CS 30306–132 to stars with strong Ba lines, while we adopted errors estimated for HD 122563 for other stars.

Finally, we derived the total uncertainty by adding, in quadrature, the individual errors, and list them in Tables 6 and 7.

4. Discussion

In this section we focus on the elemental abundances of light and heavy neutron-capture elements in metal-poor stars, which are not significantly affected by the (main) s-process, and discuss their possible origins. We first inspect the full sample based on the abundances of Sr and Ba, taken to be representative of the light and heavy neutron-capture elements, respectively, combining our new measurements with the results of previous work (subsection 4.1). Then, we confirm the similarity of the abundance patterns of light neutron-capture elements in VMP stars with high and low abundances of heavy neutron-capture elements (subsection 4.2). Since the measured abundances of Sr and Ba are, unfortunately, rather uncertain, because of the strengths of the resonance lines, particularly in stars with high abundances of neutron-capture elements, we investigate the abundances of Y, Zr, and Eu in detail for stars having relatively high abundances of neutron-capture elements (subsection 4.3).

4.1. Sr and Ba abundances

As mentioned in Section 1, Sr and Ba abundances in VMP stars exhibit remarkably large scatter; even the Sr/Ba ratio has a large scatter. Though the scatter in Sr/Ba ratios appears to be somewhat larger at lower metallicity, the behavior is unclear, in particular at $[\text{Fe}/\text{H}] < -3.5$ where the sample is still very small.

Previous studies (e.g., Truran et al. 2002, Paper II) have shown that the Sr/Ba ratio exhibits a correlation with the abundance of Ba (i.e., heavy neutron-capture elements), and the scatter is larger at lower Ba abundance in metal-poor stars. Figure 8 shows the abundances of Sr and Ba for our sample and others from previous studies, in which stars with $[\text{Fe}/\text{H}] > -2.5$ are excluded to select only VMP stars to which contributions of the main s-process are small. The same diagram was shown in Paper II, but our new sample increases the number of stars with low Ba abundances. We here adopt the values of $\log \epsilon(\text{X})$, rather than $[\text{X}/\text{Fe}]$, because the abundances of neutron-capture elements do not show a clear correlation with Fe abundance. Moreover, abundances of VMP stars are usually expected to be determined by a quite limited number of nucleosynthesis events. If this is true, the abundance ratio relative to Fe is less meaningful, and indeed makes the discussion more complicated. We discuss the correlation with metallicity (Fe abundance) later in this section.

As already shown in Paper II, the diagram of Sr and Ba abundances (Figure 8) clearly demonstrates (1) the absence of Ba-enhanced stars with low Sr abundance, and (2) the larger scatter in Sr abundances at lower Ba abundance.⁷ The former result implies that the process that produces heavy neutron-capture elements like Ba also forms light neutron-capture elements such as Sr. This gives a strong constraint on the modeling of the r-process yielding heavy neutron-capture elements, often referred to as the "main" r-process (e.g., Truran et al. 2002).

The distribution of the Sr and Ba abundances in Figure 8 can be naturally explained by assuming two nucleosynthesis processes. One produces both Sr and Ba, while the other produces Sr with little Ba, as already discussed in Paper II. In order to investigate this point in more detail, we show Sr-Ba diagrams separately for three metallicity ranges: $[\text{Fe}/\text{H}] \leq -3.1$, $-3.1 < [\text{Fe}/\text{H}] \leq -2.9$, and $[\text{Fe}/\text{H}] > -2.9$ (Figure 9). As can be seen in these figures, the stars with lowest Fe abundances have very low Ba abundances, while the Ba-rich stars appear at around $[\text{Fe}/\text{H}] \sim -3$, and then all stars with $[\text{Fe}/\text{H}] > -2.9$ have relatively high Ba abundances. This suggests that the main r-process operates only at $[\text{Fe}/\text{H}] \gtrsim -3$, and the effect is more or less seen in all stars with higher metallicity. Similar points have already been made by previous papers (e.g., Wasserburg & Qian 2000) to explain the large scatter of Ba abundances in stars at $[\text{Fe}/\text{H}] \sim -3$. An important result of the present analysis is that the scatter of Sr abundances persists even in the lowest metallicity regime. In other words, the presumed second process that produces Sr with little Ba operates even at $[\text{Fe}/\text{H}] < -3$. This is a clear difference of this process from the main r-process, which apparently did not significantly affect this metallicity range.

We note that the three stars with $[\text{Fe}/\text{H}] \sim -4$ studied by Francois et al. (2003) have very low abundances of *both* Sr and Ba. The $[\text{Fe}/\text{H}] \sim -4$ star CS 22949-037 has a relatively high Sr abundance ($\log \epsilon(\text{Sr}) = -0.72$, Depagne et al. 2002). However, the high abundances of C, N, O, and α -elements relative to Fe found in this star mean that Fe is not a good metallicity indicator for this object. If this object is excluded, all stars with high Sr abundances in the most metal-poor group (top panel of Figure 9) have $[\text{Fe}/\text{H}] \gtrsim -3.5$. This may be another constraint on the process producing light neutron-capture elements at very low metallicity. However, the sample is still too small, and further measurements of Sr and Ba abundances at $[\text{Fe}/\text{H}] < -3.5$ are strongly desired.

The above inspection demonstrates that the process forming both light and heavy neutron-capture elements (the main r-process) appears only for stars with $[\text{Fe}/\text{H}] \gtrsim -3$, while another process producing light neutron-capture elements appears at even lower metallicity. This metallicity dependence is important information to constrain the progenitor stars responsible for such events. However, there exists some controversy on the implication of the metallicity of these stars. In this metallicity range, no clear age-metallicity relation can be assumed, since the metal enrichment is expected to be strongly dependent on the nature of the previous-generation stars and the formation

⁷Some CEMP-s stars exhibit very high Ba abundances with a moderate excess of Sr (e.g., LP 706-7 = CS 31062-012: $\log \epsilon(\text{Ba}) = 1.65$, and $\log \epsilon(\text{Sr}) = 0.67$; Aoki et al. 2002b). These stars are excluded from our sample, as mentioned in the caption of Figure 8.

processes of the low-mass stars we are currently observing.

One possibility is that the metallicity indicates the sequence of mass of the progenitor stars that contributed to the next generation low-mass stars. Tsujimoto, Shigeyama & Yoshii (2000) suggested that lower-metallicity stars reflect the yields of supernovae whose progenitor mass is lower, on the basis of the theoretical prediction that supernovae from lower mass progenitors yield smaller amount of metals.⁸ The high abundances of light neutron-capture elements in some stars in the lowest metallicity range indicate that these elements were provided by supernovae with even lower-mass progenitors, while the main r-process is related to progenitors with $20 M_{\odot}$, according to Tsujimoto, Shigeyama & Yoshii (2000). On the other hand, the lower metallicity might result from the higher explosion energy of type II supernovae, which swept up larger amounts of interstellar matter and induced the formation of next-generation stars with lower metallicity. If higher-mass progenitor stars explode with higher energy, the existence of stars with high abundances of light neutron-capture elements at very low metallicity indicates that the process responsible for these elements is related to very massive stars.

Because of the difficulties noted above, interpretations of the metallicity dependence of the processes producing light and/or heavy neutron-capture elements are still premature. Although our results provide constraints on such models, further investigation of each process is required. In particular, detailed chemical abundance studies of stars having high abundances of neutron-capture elements would be very useful. Previously, several stars with large overabundances of heavy neutron-capture elements have been studied in great detail (e.g., Sneden et al. 1996; Cayrel et al. 2001), providing strong constraints on models of the main r-process. By way of contrast, studies for stars with low Ba and high Sr abundances are still quite limited to date. Studies of the detailed abundance patterns of such objects, as has been made for stars with excesses of heavy r-process elements like CS 22892–052 (Sneden et al. 2003) and CS 31082–001 (Hill et al. 2002), will provide a definitive constraint on modeling the presumed additional process that creates the light neutron-capture elements in the early Galaxy.

4.2. Abundance Ratios of Light Neutron-Capture Elements

In the previous section we investigated the correlation between the abundances of Sr and Ba, which are detected in almost all stars in our sample. In this section we investigate the abundance ratios of the three light neutron-capture elements Sr, Y, and Zr ($[\text{Sr}/\text{Y}]$ and $[\text{Y}/\text{Zr}]$).

Figure 10 shows the values of $[\text{Sr}/\text{Y}]$ and $[\text{Y}/\text{Zr}]$ as functions of $[\text{Ba}/\text{H}]$ for stars with $[\text{Fe}/\text{H}] < -2.5$. Since Y and Zr are detected only in stars with relatively high Sr abundances, stars

⁸Tsujimoto, Shigeyama & Yoshii (2000) adopted $[\text{Mg}/\text{H}]$ as a metallicity indicator, while our discussion makes use of $[\text{Fe}/\text{H}]$. However, the $[\text{Mg}/\text{Fe}]$ ratio is almost constant in most stars in this metallicity range, as seen in subsection 3.3.

with very low Sr abundance, which are located at the lower left in Figure 8, are not included in Figure 10. Therefore, the stars with high $[\text{Ba}/\text{H}]$ reflect the results of the main r-process, while the other process that produces light neutron-capture elements with little heavier species is presumed to be responsible for stars with low $[\text{Ba}/\text{H}]$ values in this figure. The lower panel of Figure 10 shows no clear dependence of $[\text{Y}/\text{Zr}]$ on $[\text{Ba}/\text{H}]$, indicating that these two processes produce very similar abundance ratios of light neutron-capture elements. The average value of $[\text{Y}/\text{Zr}]$ for the 7 stars in our sample in which both Y and Zr are detected is $\langle [\text{Y}/\text{Zr}] \rangle = -0.44$, while that of the all stars shown in the figure (29 stars) including objects studied by previous work is -0.38 .

The Y and Zr abundance ratios in VMP stars have been investigated by Johnson & Bolte (2002) in some detail. These authors found no correlation between $[\text{Y}/\text{Zr}]$ and $[\text{Fe}/\text{H}]$ in the very low metallicity range. This means that there is no correlation between $[\text{Y}/\text{Zr}]$ and the abundances of heavy neutron-capture elements, because their sample includes stars with both high and low abundances of Ba. Figure 10 shows this result more clearly, by increasing the sample of VMP stars and by adopting the Ba abundance, instead of Fe, as the horizontal axis.

Since the main component of the s-process is the dominant contributor to Y and Zr in solar-system material (e.g., Arlandini et al. 1999), the $[\text{Y}/\text{Zr}]$ ratio yielded by this process is similar to the solar-system one ($[\text{Y}/\text{Zr}]_{\text{main-s}} \sim 0$). This is clearly different from the $[\text{Y}/\text{Zr}]$ value found in the VMP stars shown in Figure 10. The weak component of the s-process, which was introduced to explain the excess of light s-process nuclei in the Solar System, is a candidate for the process responsible for the stars with large excesses of light neutron-capture elements relative to the heavier ones. However, the yields of elements produced by this process rapidly decreases with increasing mass number at around $A \sim 90$. Indeed, the $[\text{Y}/\text{Zr}]$ ratio predicted by Raiteri et al. (1993) for the weak s-process is $[\text{Y}/\text{Zr}]_{\text{weak-s}} = +0.3$, which cannot explain the observational results for VMP stars.

The $[\text{Y}/\text{Zr}]$ ratio predicted for the r-process component in the Solar System, estimated by Arlandini et al. (1999), is $[\text{Y}/\text{Zr}]_{\text{r-ss}} \sim -0.3$, which agrees well with the values found for VMP stars. This suggests that the light neutron-capture elements in VMP stars, including objects with large excesses of light neutron-capture elements relative to heavy ones, originated from the r-process, although the r-process fraction of these light neutron-capture elements is still quite uncertain.⁹ The predictions of this abundance ratio by existing models of the r-process exhibit rather large variations (Woosley et al. 1994; Wanajo et al. 2002, 2003), presumably reflecting the uncertainties of nuclear data and wide range of parameters of models such as the electron fraction. The small scatter in the Y/Zr ratios found in the VMP stars suggests the existence of some mechanisms that regulate this abundance ratio. The abundance ratio of Y/Zr in these stars and its small scatter could be strong constraints on the modeling of the r-process nucleosynthesis.

⁹Indeed, the decomposition of solar-system abundances by Burris et al. (2000) indicates a larger fraction of the r-process component for Y, resulting in $[\text{Y}/\text{Zr}]_{\text{r-ss}} = 0.17$, much higher than found in r-process element-enhanced stars (see Hill et al. 2002).

The upper panel of Figure 10 shows $[\text{Sr}/\text{Y}]$ as a function of $[\text{Ba}/\text{H}]$. The bulk of stars have $0.0 \leq [\text{Sr}/\text{Y}] \leq +0.50$, but the scatter is much larger than that observed in $[\text{Y}/\text{Zr}]$. This may reflect the large errors in Sr abundance measurements caused by the limited number of lines used for the measurements and the difficulty in the analysis of strong resonance lines. Given such relatively large uncertainties, we can only claim that the $[\text{Sr}/\text{Y}]$ value is constant within a range of ~ 0.3 dex. Johnson & Bolte (2002) also investigated the $[\text{Sr}/\text{Y}]$ ratios in metal-poor stars, and suggested a constant value of $[\text{Sr}/\text{Y}]$ with a relatively large scatter.

In Figure 11, we show for completeness the $[\text{Ba}/\text{Eu}]$ ratios, which have been studied in detail by previous studies (e.g., McWilliam 1998). The average of the $[\text{Ba}/\text{Eu}]$ values is ~ -0.6 , agreeing with the ratio of the r-process component in solar-system material. This indicates again that the neutron-capture elements, at least the heavy ones, in these metal-poor stars are dominated by the products of the r-process.

4.3. Ba-Enhanced stars

In this section we investigate the correlation between the abundances of light and heavy neutron-capture elements, adopting Y, Zr and Eu abundances as indicators, rather than the Sr and Ba abundances. The first two elements represent the light neutron-capture elements, while Eu represents the heavy neutron-capture elements. Since the absorption lines of Y II, Zr II, and Eu II are much weaker than the resonance lines of Sr II and Ba II, the abundances of Y, Zr, and Eu are only determined for stars having relatively high abundances of neutron-capture elements. However, the uncertainties of abundance measurements for these three elements are smaller than those for Sr and Ba in general. Therefore, Y, Zr, and Eu are good probes to investigate the light and heavy neutron-capture elements in neutron-capture-element-rich stars.

The upper and lower panels of Figure 12 show the abundances of Y and Zr, respectively, as functions of the Eu abundance. The typical abundance ratio of $N_{\text{Ba}}/N_{\text{Eu}}$ in these stars is ~ 10 , corresponding to $[\text{Ba}/\text{Eu}] \sim -0.7$. Hence, the distribution of Eu abundance from $\log \epsilon(\text{Eu}) = -3$ to -1 corresponds to that of the Ba abundance from $\log \epsilon(\text{Ba}) = -2$ to 0 in Figure 8. The Y and Zr abundances show clear correlations with the Eu abundance, in particular in the range $\log \epsilon(\text{Eu}) > -2$. The scatter seen in these diagrams is much smaller than that in the Sr–Ba diagram (Figure 8), even if we limit the discussion to stars with high Ba abundances. The tight correlation between the Y (Zr) and Eu abundances suggests that the scatter of Sr (and Ba) abundances found in the stars with high Ba abundances in the Sr–Ba diagram is, at least partially, caused by measurement errors in Sr and/or Ba. It should be noted that, even if errors of abundance measurements are included, the very large (> 2 dex) scatter in the Sr abundances among stars with low Ba abundances remains.

The slope of the correlation found in the Y–Eu and Zr–Eu diagrams is very interesting. Since these are diagrams of logarithmic abundances, the increase of both elements with a fixed ratio (on

a linear scale) results in a line with a slope of unity, and the change of the ratio appears only as a parallel shift of the line. Since stars with extremely low metallicity ($[\text{Fe}/\text{H}] < -2.5$) are treated here, their abundances of neutron-capture elements are expected to have been determined by a quite limited number of processes (Audouze & Silk 1995). The large scatter in the abundances ($\log \epsilon$ values) of neutron-capture elements is interpreted as a result of variation in the amount of yields by individual supernovae, and subsequent dilution by interstellar matter. If the interstellar matter contains almost no neutron-capture elements, the dilution does not change the abundance ratios between neutron-capture elements, while that changes their total abundances (relative to hydrogen). If we assume fixed abundance ratios between light and heavy neutron-capture elements, the slope found in Figure 12 should be unity. However, a correlation with a slope of $\sim 1/2$ is found in the figure. The line with a slope of $1/2$ is formed by the increase of abundances with a relation of $y \propto x^{1/2}$ (e.g., $N_Y \propto N_{\text{Eu}}^{1/2}$). Such a behavior is quite unexpected, if the abundances of neutron-capture elements relative to hydrogen are determined by the yields from explosive processes like supernovae and the dilution by interstellar matter that contains no neutron-capture elements. Moreover, the scatter is larger at lower Eu abundances.

How might we explain the observed distribution of Y and Eu abundances? If we assume two processes, which produce different ratios of $\text{Y}(\text{Zr})/\text{Eu}$, some insight can be obtained. The solid lines in the upper panel of Figure 12 indicate the increase of Eu and Y abundances with a fixed ratio of $\delta N_Y/\delta N_{\text{Eu}} = 5$, assuming two different initial values ($\log \epsilon(\text{Y}) = -0.5$ and -2.8 at $\log \epsilon(\text{Eu}) = -3.5$). Most stars in the diagram can be explained by changing the initial Y abundances between these two values. The dotted lines correspond to the case of $\delta N_Y/\delta N_{\text{Eu}} = 2$ and initial values of $\log \epsilon(\text{Y}) = -0.2$ and -3.2 at $\log \epsilon(\text{Eu}) = -3.5$. The large cross in the figure indicates the values of the r-process component for these elements in the Solar System (Arlandini et al. 1999), which can also be explained by the increase of Y and Eu in such a manner, although it must be kept in mind that the r-process contribution to solar-system material for light neutron-capture elements is still somewhat uncertain.

One might intuit that the increase of Y abundances with respect to Eu with a fixed ratio corresponds to enrichment by the main r-process, while the initial values assumed above are determined by the process that produced light neutron-capture elements with little accompanying heavy species. If this is true, the neutron-capture elements in stars near the line with a slope of unity are provided by the main r-process, while all other stars are more or less affected by the process that produces light neutron-capture elements. The above comparisons of solid and dotted lines with data points indicate that the main r-process produces the Y/Eu abundance ratio of $\delta N_Y/\delta N_{\text{Eu}} = 2 \sim 5$, while another process yields these elements with a quite large distribution (~ 2 dex) in the ratio.

The solid and dotted lines in the lower panel of Figure 12 indicates the increase of Zr and Eu abundances with a fixed ratio of $\delta N_{\text{Zr}}/\delta N_{\text{Eu}} = 20$ and 10 , respectively, assuming two different initial values. The Zr and Eu abundances of metal-poor stars as well as that of the r-process component in the Solar System (Arlandini et al. 1999), indicated by the cross in this figure, can also be explained by changing the initial $[\text{Zr}/\text{Eu}]$ ratio.

In the above discussion, the effect of the nucleosynthesis process producing light neutron-capture elements is regarded as the source of the difference of the “initial values” of Y and Zr. However, this does not necessarily mean that these processes have operated in advance of the main r-process. The time scale of the contribution of each process is dependent on the progenitor mass, which is still unclear, as discussed in subsection 4.1. While a fixed abundance ratio of [Y/Eu] and [Zr/Eu] can be assumed for the main r-process, large distributions of these abundance ratios are required for the other process to explain the large scatter in the Y and Zr abundances at low Eu abundance. Further observational studies to determine the elemental abundance patterns produced by this process, covering a wider atomic number range, are clearly required.

5. Summary and Concluding Remarks

We have measured elemental abundances for 18 very metal-poor stars using spectra obtained with the Subaru Telescope High Dispersion Spectrograph. The metallicity range covered by our sample is $-3.1 \lesssim [\text{Fe}/\text{H}] \lesssim -2.4$. While the abundances of carbon, α -elements, and iron-peak elements determined for these stars show similar trends to those found by previous work, we found an exceptional star, BS 16934–002, a giant with $[\text{Fe}/\text{H}] = -2.8$ having large over-abundances of Mg, Al and Sc. Further abundance studies for this object are strongly desired.

By combining our new results with those of previous studies, we investigated the distribution of neutron-capture elements in very metal-poor stars, focusing on the production of the light neutron-capture elements (Sr, Y, and Zr), and found the following observational results:

- (1) A large scatter is found in the abundance ratios between the light and heavy neutron-capture elements (e.g., Sr/Ba) for stars with low abundances of heavy neutron-capture elements. Most of these stars have extremely low metallicity ($[\text{Fe}/\text{H}] \lesssim -3$).
- (2) Stars with high abundances of heavy neutron-capture elements appear in the metallicity range of $[\text{Fe}/\text{H}] \gtrsim -3$. The observed scatter in the ratios between light and heavy neutron-capture elements is much smaller in these stars. In particular, the Y and Zr abundances exhibit a clear correlation with Eu abundance in stars with high Eu abundances, but the trend is not explained by the increases of light and heavy elements with fixed abundance ratios.
- (3) The Y/Zr ratio is similar in stars with high and low abundances of heavy neutron-capture elements. The values of the [Y/Zr] indicate these are not products of the main nor weak components of the s-process, but must have an origin related to the r-process.

These observational results indicate the existence of the process that yielded light neutron-capture elements (Sr, Y, and Zr) with little contribution to heavy ones (e.g., Ba, Eu). This process seems to be different from the weak s-process. Such a process has been suggested by previous studies (e.g., Truran et al. 2002; Johnson & Bolte 2002; Travaglio et al. 2004), as mentioned in Section 1. The above results suggest that this process appears even in extremely metal-poor

stars ($[\text{Fe}/\text{H}] \sim -3.5$), but is seen as well in stars with higher metallicity and higher abundances of heavy neutron-capture elements. The ratios of light to heavy neutron-capture elements (e.g., Sr/Ba, Y/Eu) formed by this process have a wide distribution, while the abundance ratios of elements among light neutron-capture elements (e.g., Y/Zr), as well as those among heavy ones (e.g., Ba/Eu), are almost constant.

These observational results provide new constraints on modeling r-process nucleosynthesis, and identifying its likely astrophysical sites. However, further observational studies are required. In particular, measurements for lower metallicity stars ($[\text{Fe}/\text{H}] < -3.5$) are very important to understand the process that produced light neutron-capture elements in the very early Galaxy. More detailed abundance studies for stars showing large excesses of light neutron-capture elements, with low abundances of heavier ones, will provide definitive constraints on the modeling of that process.

T.C.B. acknowledges partial support from a series of grants awarded by the US National Science Foundation, most recently, AST 04-06784, as well as from grant PHY 02-16783; Physics Frontier Center/Joint Institute for Nuclear Astrophysics (JINA).

REFERENCES

- Alonso, A., Arribas, S., & Martínez-Roger, C. 1994, *A&AS*, 107, 365
- Alonso, A., Arribas, S., & Martínez-Roger, C. 1999, *A&AS*, 140, 261
- Arlandini, C., Käppeler, F., Wisshak, K., Gallino, R., Lugaro, M., Busso, M., & Straniero, O. 1999, *ApJ*, 525, 886
- Aoki, W., Norris, J.E., Ryan, S.G., Beers, T.C., & Ando, H. 2002a, *ApJ*, 576, L141
- Aoki, W., Ryan, Norris, J.E., S.G., Beers, T.C., Ando, H., & Tsangarides, S. 2002b, *ApJ*, 580, 1149
- Aoki, W., Norris, J. E., Ryan, S. G., Beers, T.C., Christlieb, N., & Ando, H. 2004, *ApJ*, 608, 971
- Aoki, W., & Tsuji, T. 1997, *A&A*, 317, 845
- Audouze, J., & Silk, J. 1995, *ApJ*, 451, L49
- Beers, T.C. 1999, in *Third Stromlo Symposium: The Galactic Halo*, eds. B. Gibson, T. Axelrod, & M. Putman (ASP: San Francisco), 165, p. 206
- Beers, T.C., Preston, G.W., & Shectman, S.A. 1985, *AJ*, 90, 2089
- Beers, T.C., Preston, G.W., & Shectman, S.A. 1992, *AJ*, 103, 1987
- Bessell, M. S., & Norris, J. E. 1984, *ApJ*, 285, 622

- Burris, D. L., Pilachowski, C. A., Armandroff, T. E., Sneden, C. Cowan, J. J., & Roe, H. 2000, *ApJ*, 544, 302
- Carpenter, J. M. 2001, *AJ*, 121, 2851
- Carretta, E., Gratton, R., Cohen, J. G., Beers, T. C., & Christlieb, N. 2002, *AJ*, 124, 481
- Carretta, E., Gratton, R., & Sneden, C. 2000, *A&A*, 356, 238
- Cayrel, R. et al. 2001, *Nature*, 409, 691
- Cayrel, R., Depagne, E., Spite, M., Hill, V., Spite, F., Francois, P., Plez, B., Beers, T.C., Primas, F., Andersen, J., Barbuy, B., Bonifacio, P., Molaro, P., & Nordström, B. 2004, *A&A*, 416, 1117
- Cohen, J. G., Christlieb, N., McWilliam, A., Shectman, S., Thompson, I., Wasserburg, G. J., Ivans, I., Dehn, M., Karlsson, T., & Melendez, J. 2004, *ApJ*, 612, 1107
- Depagne, E., et al. 2002, *A&A*, 390, 187
- Fernie, J. D. 1983, *PASP*, 95, 782
- François, P. et al. 2003, *A&A*, 403, 1105
- Honda, S. et al. 2004a, *ApJS*, 152, 113
- Honda, S., Aoki, W., Kajino, T., Ando, H., Beers, T. C., Izumiura, H., Sadakane, K., & Takada-Hidai, M. 2004b, *ApJ*, 607, 474
- Hill, V. et al. 2002, *A&A*, 387, 560
- Irwin, A. W. 1981, *ApJS*, 45, 621
- Ishimaru, Y., Wanajo, S., Aoki, W., & Ryan, S. G. 2004, *ApJ*, 600, L47
- Johnson, J. A. 2002, *ApJS*, 139, 219
- Johnson, J. A., & Bolte, M. 2002, *ApJ*, 579, 616
- Kurucz, R. L., 1993, CD-ROM 13, ATLAS9 Stellar Atmospheres Programs and 2 km/s Grid (Cambridge: Smithsonian Astrophys. Obs.)
- Lawler, J. E., Bonvallet, G., & Sneden, C. 2001a, *ApJ*, 556, 452
- Lawler, J. E., Wickliffe, M. E., Den Hartog, E. A., & Sneden, C. 2001b, *ApJ*, 563, 1075
- McWilliam, A., Preston, G. W., Sneden, C., & Searle, L. 1995, *AJ*, 109, 2757
- McWilliam, A. 1998, *AJ*, 115, 1640

- Noguchi, K., Aoki, W., Kawanomoto, S., et al. 2002, PASJ, 54, 855
- Norris, J.E., Ryan, S.G., & Beers, T.C. 1996, ApJS, 107, 391
- Norris, J. E., Ryan, S. G., & Beers, T. C. 2001, ApJ, 561, 1034
- Press, W. H., Teukolsky, S. A., Vetterling, W. T., & Flannery, B.P. 1996, Numerical Recipes in Fortran 77, second edition, Cambridge
- Raiteri, C. M., Gallino, R., Busso, M., Neuberger, D., & Käppeler, F. 1993, ApJ, 419, 207
- Ryan, S.G., Norris, J.E., & Beers, T.C. 1996, ApJ, 471, 254
- Schlegel, D.J., Finkbeiner, D.P., & Davis, M. 1998, ApJ, 500, 525
- Simmerer, J., Sneden, C., Cowan, J. J., Collier, J. Woolf, V. M., & Lawler, J. E. 2004, ApJ, 617, 1091
- Skrutskie, M.F., et al. 1997, in The Impact of Large Scale Near-IR Sky Surveys, ed. F. Garzon et al. (Dordrecht: Kluwer), p. 187
- Sneden, C., McWilliam, A., Preston, G.W., Cowan, J.J., Burris, D., & Armosky, B.J. 1996, ApJ 467, 819
- Sneden, C., Cowan, J. J., Ivans, I. I., Fuller, G. M., Burles, S., Beers, T. C., & Lawler, J. E. 2000, ApJ, 533, L139
- Sneden, C. et al. 2003, ApJ, 591, 936
- Spite, M. et al. 2005, A&A, 430, 655
- Travaglio, C., Gallino, R. Arnone, E., Cowan, J., Jordan, F., & Sneden, C. 2004, ApJ, 601, 864
- Truran, J. W., Cowan, J. J., Pilachowski, C. A., & Sneden, C. 2002, PASP, 114, 1293
- Tsujimoto, T., & Shigeyama, T. 2003, ApJ, 584, L87
- Tsujimoto, T., Shigeyama, T., & Yoshii, Y. 2000, ApJ, 531, L33
- Umeda, H., & Nomoto, K. 2003, Nature, 422, 871
- Unsöld, A., 1955, Physik der Sternatmosphären (2nd ed., Berlin: Springer)
- Wanajo, S., Itoh, N., Ishimaru, Y., Nozawa, S. & Beers, T. C. 2002, ApJ, 577, 853
- Wanajo, S., Tamamura, M., Itoh, N., Nomoto, K., Ishimaru, Y., Beers, T. C., & Nozawa, S. 2003, ApJ, 593, 968
- Wasserburg, G. J., & Qian, Y.-Z. 2000, ApJ, 529, L21

Westin, J., Sneden, C., Gustafsson, B., & Cowan, J.J. 2000, ApJ, 530, 783

Woosley, S. E., Wilson, J. R., Mathews, G. J., Hoffman, R. D., & Meyer, B. S. 1994, ApJ, 433, 229

Table 1. OBJECT LIST AND OBSERVING LOG

ID	Object name	RA(2000)	Dec(2000)	Exposure (min)	S/N ^a	Obs. Date (JD) (km s ⁻¹)	Radial velocity
1	HD122563	14 02 31.8	+09 41 10	15	1500	2 Feb. 2002	-25.81 ± 0.17
2	BS 16033-008	13 05 56.1	+25 10 17	60	100	16 Apr. 2001	-30.43 ± 0.27
3	BS 16080-054	16 39 18.5	+60 57 42	20	89	23 July 2001	-120.80 ± 0.25
4	BS 16083-172	14 50 41.6	+48 45 14	40	86	31 July 2001	-165.41 ± 0.33
5	BS 16084-160	16 28 50.7	+54 37 03	40	102	23 July 2001	-118.71 ± 0.24
6	BS 16089-013	13 49 22.1	+35 44 53	40	86	31 July 2001	-257.18 ± 0.31
7	BS 16543-097	13 26 28.3	+21 38 42	40	164	14 Apr. 2001	-24.57 ± 0.21
8	BS 16934-002	13 29 46.4	+16 15 39	20	63	16 Apr. 2001	+82.81 ± 0.26
				30	84	31 July 2001	+82.53 ± 0.26
				30	82	2 Feb. 2002	+82.33 ± 0.21
9	BS 17439-065	11 01 20.2	-13 38 40	60	130	2 Feb. 2002	+372.21 ± 0.30
10	CS 22886-042	22 20 25.9	-10 23 20	40	91	31 July 2001	-221.36 ± 0.32
11	CS 29516-041	22 21 48.7	+02 28 48	40	135	31 July 2001	-138.19 ± 0.31
12	CS 30306-132	15 14 18.6	+07 27 02	30	129	14 Apr. 2001	-108.71 ± 0.16
				75	166	26 July 2001	-108.46 ± 0.29
13	CS 30312-059	15 34 48.8	-01 23 38	60	144	23 July 2001	-155.94 ± 0.21
14	CS 30319-020	21 19 39.6	-26 52 40	40	125	31 July 2001	+69.77 ± 0.30
15	CS 30325-028	15 05 19.8	+06 17 05	30	116	14 Apr. 2001	-148.22 ± 0.17
				30	129	2 Feb. 2002	-145.82 ± 0.12
16	CS 30325-094	14 54 39.3	+04 21 38	20	139	14 Apr. 2001	-157.64 ± 0.25
17	CS 30327-038	22 00 17.5	-33 50 06	54	122	31 July 2001	-11.19 ± 0.36
18	CS 30329-004	15 48 42.0	-06 52 43	20	132	23 July 2001	+40.23 ± 0.25

^aS/N ratio per resolution element (6 km s⁻¹) estimated from the photon counts at 4000 Å (see text)

Table 2. PHOTOMETRIC DATA

Object name	B	V	R	I	J	H	K	$E(B - V)$	$T_{\text{eff}}(V - K)_0$	$\Delta(T_{\text{eff}})^{\text{a}}$
HD 122563 ^b	7.11	6.20	5.65	5.11	4.79	4.03	3.73	0.00	4605	-11
BS 16033-008	14.416	13.786	13.367	12.943	12.327	11.881	11.831	0.01	5240	-14
BS 16080-054	13.550	12.776	12.285	11.786	11.082	10.604	10.504	0.00	4811	-5
BS 16083-172	14.058	13.434	13.025	12.594	11.991	11.578	11.496	0.01	5264	4
BS 16084-160	14.002	13.144	12.630	12.103	11.358	10.849	10.740	0.00	4670	-33
BS 16089-013	14.065	13.314	12.842	12.333	11.677	11.208	11.119	0.00	4898	62
BS 16543-097	13.261	12.570	12.113	11.657	11.009	10.542	10.463	0.01	5038	-19
BS 16934-002	13.733	12.806	12.239	11.670	11.467	10.348	10.233	0.00	4524	-15
BS 17439-065	14.141	13.434	12.993	12.518	11.880	11.438	11.370	0.02	5130	67
CS 22886-042	14.094	13.263	12.757	12.259	11.521	11.025	10.920	0.04	4863	-25
CS 29516-041	13.356	12.706	12.240	11.770	11.158	10.727	10.648	0.04	5221	69
CS 30306-132	13.605	12.867	12.421	11.948	11.278	10.844	10.746	0.01	5021	28
CS 30312-059	13.904	13.101	12.596	12.065	11.305	10.826	10.723	0.08	4960	2
CS 30319-020	13.472	12.722	12.137	11.720	11.140	10.686	10.582	0.06	5190	75
CS 30325-028	13.640	12.868	12.387	11.893	11.207	10.709	10.626	0.01	4877	5
CS 30325-094	13.019	12.317	11.849	11.376	10.682	10.234	10.130	0.04	5049	-49
CS 30327-038	13.780	13.130	11.634	11.212	11.113	0.00	5115	...
CS 30329-004	12.699	11.883	11.367	10.817	10.034	9.558	9.449	0.12	5035	1

$$^{\text{a}}\Delta(T_{\text{eff}}) = T_{\text{eff}}(V - K)_0 - \langle T_{\text{eff}}(B - V)_0, T_{\text{eff}}(V - R)_0, T_{\text{eff}}(V - I)_0, T_{\text{eff}}(R - I)_0 \rangle$$

^b R and I data are adopted from Bessell & Norris (1984), while others are from Honda et al. (2004b).

Table 3. EQUIVALENT WIDTHS

	λ (Å)	χ	$\log gf$ (eV)	$W(\text{mÅ})$																		^a
				1	2	3	4	5	6	7	8	9	10	11	12	13	14	15	16	17	18	
Mg I	3829.35	2.71	-0.21	182.1	119.2	157.9	154.6x134.2	156.3	149.7	200.9x183.0	170.1	124.6	168.4	135.3	157.2	155.1x129.0	166.9	158.1				
Mg I	3832.30	2.71	0.14	...	135.3	183.3	...	146.2	188.5	...	228.3x200.6	...	152.6	191.0	161.6	197.0	184.9x147.9	177.6	183.0			
Mg I	3986.75	4.35	-1.03	35.4	24.0	62.9x			
Mg I	4057.50	4.35	-0.89	39.5	...	32.8	33.4	27.9	71.3	...	36.8	...	43.3	15.7	32.9	32.7	11.2	34.0	32.1	
Mg I	4167.27	4.35	-0.77	55.2	...	43.3	47.7	17.9	41.6	46.7	85.3	53.8	51.2	23.9	62.6	29.0	48.5	...	18.9	38.7	40.1	
Mg I	4571.10	0.00	-5.69	85.0	10.5	45.0	31.3	28.1	41.7	42.6	115.5	41.4	60.4	14.1	58.0	23.4	46.4	52.7	19.9	31.6	31.8	
Mg I	4702.99	4.35	-0.52	75.5	...	59.7	61.5	34.9	54.4	58.6	110.5	71.5	64.9	33.5	75.9	41.2	63.6	63.4	32.0	62.6	59.1	
Mg I	5172.69	2.71	-0.38	208.9	129.9	181.0	175.3	147.8	168.4	170.4	248.9x196.7	183.9	133.5	189.1	148.0	181.9	176.1	137.3	168.1	173.6		
Mg I	5183.60	2.72	-0.16	234.2	143.7	197.6	197.9	169.1	186.3	191.5	271.0x216.3	205.4	153.1	213.2	166.1	199.5	195.9	160.4	182.4	19...		
Al I	3944.01	0.00	-0.64	163.0x111.6x125.3	131.8x12...	125.3x...	100.6	...	121.8x...	...	100.6x104.7	110.7					
Al I	3961.52	0.01	-0.34	139.0	73.6	119.3	103.6	105.5	102.7	106.9	153.3	116.2	114.6	73.5	121.3	87.7	110.2	116.9	88.4	108.9	108.1	
Si I	3905.52	1.91	-0.98	196.6	...	171.5	173.6	171.3	174.2x...	192.4	138.2	...	152.2	181.3	...	156.9	156.6	162.7		
Si I	4102.94	1.91	-2.91	90.6	...	69.2	...	66.9	55.4	67.5	8...	76.4	65.8	...	72.0	47.7	70.2	...	60.9	...	60.2	
Ca I	4226.73	0.00	0.24	200.6	133.0	175.3	171.8x158.9	157.0	164.5	201.5x188.5	18...	127.6	195.4	149.2	184.4	176.5	136.0	161.5	170.9			
Ca I	4283.01	1.89	-0.22	61.5	...	49.0	54.8	38.5	58.4	61.1	70.2	62.6	84.2x	37.3	58.4	74.0x	26.2	39.1	52.1	
Ca I	4289.36	1.88	-0.30	52.6	24.5	39.6	41.4	20.3	41.2	42.5	51.5	52.2	52.0	19.1	55.1	22.1	43.8	44.4	14.6	28.9	35.2	
Ca I	4318.65	1.90	-0.21	52.9	...	46.7	43.7	3...	39.9	44.2	55.5	58.3	51.3	18.0	54.2	28.2	44.6	42.8	20.3	34.1	45.7	
Ca I	4355.08	2.71	-0.42	11.0	
Ca I	4425.44	1.88	-0.36	49.8	...	38.2	...	26.2	33.8	40.9	...	49.6	51.7	16.1	52.4	26.6	41.2	...	19.6	26.0	34.0	
Ca I	4434.96	1.89	-0.01	...	32.7	...	52.8	...	51.1	58.5	43.2	34.6	
Ca I	4435.69	1.89	-0.52	42.0	...	33.9	33.1	...	38.8	40.1	40.3	42.2	45.9	22.4	31.6	37.5	17.3	24.5	25.1	
Ca I	4454.78	1.90	0.26	77.8	41.6	74.0	60.6	57.3	62.6	69.4	83.3	74.8	74.8	38.7	81.5	50.1	71.1	70.7	44.5	61.5	72.1	
Ca I	4455.89	1.90	-0.53	40.4	9.0	28.3	24.0	21.1	27.7	31.1	43.8	...	38.5	15.5	44.2	16.9	31.9	32.6	12.9	22.6	30.2	
Ti I	3904.78	0.90	0.03	29.6	...	14.3	19.3	14.8	35.3	...	25.0	...	18.6	...	16.3	14.8	
Ti I	3924.53	0.02	-0.88	35.1	14.4	48.0	20.9	17.5	
Ti I	3989.76	0.02	-0.14	71.7	...	49.5	46.7	29.9	46.3	49.9	86.5	64.0	63.7	...	56.8	35.3	44.9	50.6	30.9	36.3	49.0	
Ti I	3998.64	0.05	0.00	71.5	24.2	51.7	49.3	40.1	40.5	50.2	84.2	61.3	...	29.3	54.9	37.6	...	57.0	29.0	49.9	52.7	
Ti I	4008.93	0.02	-1.02	29.5	16.3	15.4	41.4	28.5	22.7	22.3	18.9	
Ti I	4533.24	0.85	0.53	53.2	18.0	38.2	33.8	24.5	4...	38.9	...	49.3	47.8	13.6	46.6	24.7	42.4	33.3	22.0	31.8	36.1	
Ti I	4534.77	0.84	0.34	42.7	13.1	...	30.7	60.1	29.4	...	13.0	35.6	20.1	3...	25.3	17.5	23.1	28.6	
Ti I	4535.57	0.83	0.12	36.9	24.9	51.8	30.4	10.9	24.5	...	9.7	
Ti I	4681.91	0.05	-1.01	29.6	14.6	15.1	...	19.2	20.4	...	17.3	...	16.7	13.8	

Table 3—Continued

Ti I	4981.73	0.85	0.56	62.2	...	46.1	31.2	...	41.2	38.9	75.8	59.7	50.5	20.1	50.8	24.0	43.9	43.4	22.6	33.4	39.8
Ti I	4991.07	0.84	0.44	58.0	...	40.7	32.2	23.0	39.0	34.8	74.8	52.9	49.1	16.7	47.6	21.1	38.7	41.1	20.7	32.4	37.4
Ti I	4999.50	0.83	0.31	51.3	...	36.0	25.5	16.6	31.5	33.5	68.8	43.3	35.1	...	40.2	16.8	36.3	...	13.8	23.7	35.6
Ti I	5039.96	0.02	-1.13	31.2	...	16.0	24.0	11.1	51.0	20.3	7.4	15.2	12.4
Ti I	5064.65	0.05	-0.94	35.9	14.4	...	15.8	16.4	52.1	...	24.8	...	23.8	...	21.1	18.7
Ti I	5173.74	0.00	-1.06	34.2	...	15.8	18.2	52.6	22.9	20.5	...	23.0	9.7	18.0	13.4	...	11.6	...
Ti I	5192.97	0.02	-0.95	39.0	14.3	15.2	25.2	18.3	56.6	31.4	28.4	...	28.6	9.5	20.5	17.2	19.5
Ti I	5210.38	0.05	-0.83	42.5	...	19.5	22.8	...	63.4	36.7	34.1	...	29.2	...	21.2	20.1	12.4	...	23.1
Cr I	3908.76	1.00	-1.00	21.6
Cr I	4254.33	0.00	-0.11	112.9	57.8	98.7	80.3	87.1	89.2	95.3	119.1	104.9	94.7	61.1	96.8	74.1	87.0	91.7	63.3	95.2	98.6
Cr I	4274.80	0.00	-0.23	112.7	51.4	97.6	78.7	81.4	94.8	91.2	...	105.8	101.3	65.1	105.9	75.2	96.1	99.1	60.5	86.0	89.9
Cr I	4289.72	0.00	-0.36	106.0	60.5	89.2	71.6	80.7	89.1	88.2	113.6	101.4	100.2	55.8	98.4	65.0	87.7	92.4	56.3	86.2	83.2
Cr I	4344.51	1.00	-0.55	31.8
Cr I	4351.05	0.97	-1.45	12.7	13.7
Cr I	4600.75	1.00	-1.26	17.3	2...
Cr I	4616.14	0.98	-1.19	21.1	10.9	22.7	15.8	...	12.6	13.0
Cr I	4626.19	0.97	-1.32	17.5	11.4	15.8	12.5	9.7
Cr I	4646.17	1.03	-0.70	36.2	...	24.5	...	16.7	13.9	26.4	28.0	...	27.0	11.7	20.7	17.9	21.6
Cr I	4652.16	1.00	-1.03	24.7	15.6	28.7	15.6	...	14.2	13.2	9.3
Cr I	5206.04	0.94	0.02	85.6	...	64.3	...	53.1	62.0	...	91.7	83.2	77.7	33.3	72.7	...	64.9	64.1	36.5	61.5	59.7
Cr I	5208.44	0.94	0.16	86.6	...	70.9	73.0	...	111.6	113.1x...	95.4	80.7	44.2	77.1	79.0
Mn I	3823.51	2.14	0.06	16.6	11.1	18.1	7.9	9.8
Mn I	4030.75	0.00	-0.47	139.1	64.9	104.8	86.5	101.3	91.6	104.8	13...	119.7	115.9	58.1	109.0	71.7	102.4	105.9	54.8	...	96.8
Mn I	4033.06	0.00	-0.62	124.5	54.5	95.8	80.8	87.2	75.6	89.3	115.2	102.6	103.3	45.9	95.7	57.5	91.6	93.0	46.6	99.7	86.5
Mn I	4034.48	0.00	-0.81	118.0	49.2	84.4	73.8	79.2	77.9	91.5	113.2	88.3	96.0	41.4	106.2	54.4	95.2	110.9	36.9	87.4	71.7
Mn I	4041.36	2.11	0.28	44.1	23.8	31.3	38.7	32.0	...	20.1	21.7	...	28.6	19.4
Mn I	4055.55	2.14	-0.07	20.2	15.4	16.7	12.2
Mn I	4451.58	2.89	0.28	9.1	6.1	12.7
Mn I	4754.05	2.28	-0.09	2...	15.1	12.3	8.9
Mn I	4783.43	2.30	0.04	23.9	14.8	13.6	5.3	12.8	9.0	...	15.3	...
Mn I	4823.53	2.32	0.14	26.1	...	11.4	14.2	16.3	23.2
Fe I	3763.79	0.99	-0.24	...	107.0	144.7	136.6	147.7	...	149.2	117.5	151.4x127.2	147.0	151.3	111.1
Fe I	3767.19	1.01	-0.39	...	109.7	144.7	104.8	123.9	127.1	136.9	130.8	106.0	143.3	116.7	128.9	147.2	110.1	145.0	134.7
Fe I	3787.88	1.01	-0.86	144.9	94.5	131.9	89.8	124.0	101.2	109.7	134.0	126.0	...	92.1	115.1	96.6	108.7	117.5	98.4	120.5	120.6

Table 3—Continued

Fe I	3805.34	3.30	0.31	66.2	...	55.5	...	49.8	46.2	57.7	54.8	65.6	64.6	35.9	65.9	43.8	61.3	...	33.2	59.8	53.2
Fe I	3815.84	1.49	0.23	174.2	116.2	148.9	134.5	132.9	...	137.3	161.7x	164.8	153.2	116.2	153.7	121.7	149.8	142.1x	115.9	150.3	143.7
Fe I	3820.43	0.86	0.12	...	143.6	186.2	...	192.4	167.8	156.8	200.1x	167.3	149.9	189.3	183.5
Fe I	3825.88	0.92	-0.04	...	131.7	176.2	159.2x	162.7	155.5	162.8	...	182.1	...	139.4	186.3x	148.7	180.6	...	134.4	...	165.0
Fe I	3827.82	1.56	0.06	159.9	105.6	136.7	131.5	126.6	118.6	129.2	152.4	149.9	148.7	108.5	136.0	112.6	135.4	133.2	105.0	128.6	133.7
Fe I	3839.26	3.05	-0.33	50.4	...	40.1	30.5	30.5	40.4	44.7	55.0	47.1	44.4	21.4	42.2	21.5	39.3	...	19.3	42.7	41.1
Fe I	3840.44	0.99	-0.51	165.4	117.4	135.1	128.4	...	124.4	131.7	146.4	147.1	148.5	106.3	138.8	119.2	138.2	129.8	110.5	140.7	131.5
Fe I	3841.05	1.61	-0.06	144.1	90.8	125.2	11...	124.4	103.6	119.0	134.3	138.5	...	97.5	124.9	102.3	119.6	111.2	95.6	126.8	121.2
Fe I	3845.17	2.42	-1.39	44.7	19.8	19.5	...	30.4	35.6	42.0	33.0	15.5	31.8	...	13.8	26.2	22.5
Fe I	3846.41	3.57	-0.47	13.6	...	21.4	5.8	15.4	12.9	5.2
Fe I	3846.80	3.25	-0.02	55.0	...	48.2	35.4	31.0	36.3	48.4	51.0	56.7	...	27.3	...	29.9	47.3	46.2	...	48.1	40.3
Fe I	3849.98	1.01	-0.86	149.5	86.4	125.9	104.0	124.0	115.2	115.5	131.7	139.6	131.0	94.9	119.2	102.6	121.3	117.0	95.4	126.0	121.2
Fe I	3850.82	0.99	-1.75	...	63.0	108.8	75.3	97.1	...	89.1	117.6	117.6	115.2	69.6	111.1	83.2	94.3	96.8	7...	99.9	94.8
Fe I	3852.57	2.18	-1.18	71.5	30.5	60.8	42.7	47.5	56.3	53.1	63.6	72.2	70.1	25.2	68.2	32.9	62.7	51.0	24.7	49.6	44.7
Fe I	3856.37	0.05	-1.29	182.2	112.2	154.0	129.8	160.1	140.4	139.9	178.9x	168.6	159.1	115.4	147.9	128.0	...	151.6	124.3	148.2	150.2
Fe I	3859.91	0.00	-0.71	...	155.6	186.8	...	157.1	210.8	161.9	151.2	194.1	181.4
Fe I	3863.74	2.69	-1.43	39.8	24.3	31.4	23.6	18.4
Fe I	3865.52	1.01	-0.98	149.0	...	132.9	94.9	118.5	111.6	112.8	141.0	137.6	119.0	93.8	113.4	100.8	110.8	106.4	95.9	123.2	118.8
Fe I	3867.22	3.02	-0.45	46.7	...	35.5	25.1	36.5	41.6	49.7	39.3	25.4	38.0	20.4	42.0	33.6	18.1	36.4	32.8
Fe I	3883.28	3.25	-0.69	33.3	...	41.0	31.4	33.0	25.5
Fe I	3885.51	2.42	-1.09	58.6	...	29.9	42.2	29.0	...	42.5	42.5	51.7	...	22.5	43.5	21.2	39.5	37.2	19.0	37.6	30.1
Fe I	3886.28	0.05	-1.08	163.6	...	161.6	...	156.1	...	181.9	...	126.6	173.8x	144.9	162.7	168.0x	138.8	158.4	153.5
Fe I	3899.71	0.09	-1.53	172.1	110.9	149.7	112.2	142.6	133.3	130.7	156.8x	154.0	148.5	107.2	133.1	116.7	133.9	136.4	112.2	141.8	138.0
Fe I	3902.95	1.56	-0.47	136.8	83.4	110.9	95.2	109.3	112.1	109.2	118.9	136.3	121.6	88.6	109.8	96.5	116.3	113.3	87.3	120.1	113.8
Fe I	3917.18	0.99	-2.15	108.4	49.4	69.3	65.6	75.8	...	96.5	...	55.5	75.6	...	77.6	79.0	52.8	74.9	76.2
Fe I	3920.26	0.12	-1.75	161.9	101.4	146.1	102.9	137.7	122.1	121.7	156.0	142.0	123.2	97.6	121.6	109.2	126.9	127.4	105.3	126.6	133.5
Fe I	3922.91	0.05	-1.65	172.7	108.4	147.5	110.5	149.2	117.1	129.2	163.6x	153.9	140.1	108.0	133.1	124.8	128.6	134.1	113.8	140.5	133.8
Fe I	3940.88	0.96	-2.60	83.5	33.4	65.4	46.2	56.9	84.1	...	65.7	62.9	31.8	56.9	52.1
Fe I	3949.95	2.18	-1.25	67.1	...	52.4	...	43.8	46.0	50.6	73.5	62.0	58.7	...	52.9	31.6	24.5	...	48.5
Fe I	3977.74	2.20	-1.12	74.8	47.5	46.2	...	57.1	71.5	55.0	38.7	...	54.4	27.4
Fe I	4001.66	2.18	-1.90	37.7	22.8	26.5	...	23.7	23.7	13.1
Fe I	4005.24	1.56	-0.61	132.2	...	114.7	79.6	106.8	93.2	102.7	119.5	120.1	117.7	80.1	111.1	91.1	105.6	107.4	84.7	118.6	112.3
Fe I	4007.27	2.76	-1.28	28.6	16.1	31.3	15.2	14.7
Fe I	4014.53	3.05	-0.59	71.8	...	39.0	39.3	46.7	82.5x	63.5	...	21.4	51.8	...	48.5	47.9	22.1	38.0	42.9

Table 3—Continued

Fe I	4021.87	2.76	-0.73	54.2	...	41.7	32.6	28.3	36.7	39.7	...	51.7	61.7	19.1	48.7	...	44.4	40.6	20.3	41.9	39.6
Fe I	4032.63	1.49	-2.38	53.3	...	32.1	...	27.2	24.4	27.6	46.0	38.5	45.0	...	36.7	13.9	27.7	29.6	9.1	23.6	28.1
Fe I	4044.61	2.83	-1.22	31.7	...	18.1	15.5	18.5	31.1	25.7	25.2	...	26.4	15.1	...	15.0	13.7
Fe I	4058.22	3.21	-1.11	31.2	2...	21.4	...	15.6	21.3	...	15.9	11.3
Fe I	4062.44	2.85	-0.86	47.8	...	30.8	24.5	...	23.8	31.6	43.0	43.7	35.9	13.4	34.1	15.6	35.1	28.4	10.2	28.5	26.6
Fe I	4063.59	1.56	0.06	164.2	102.9	142.2	126.9	138.3	124.8	136.6	153.8	147.5	145.1	111.2	144.2	122.0	139.9	139.6	110.6	140.9	136.0
Fe I	4067.27	2.56	-1.42	41.4	25.7	22.5
Fe I	4067.98	3.21	-0.47	43.4	31.6	35.3	37.8	36.3	33.8	24.5
Fe I	4070.77	3.24	-0.79	27.5	13.1	...	18.5	22.2	22.9	22.0	...	25.3	16.0	14.7
Fe I	4071.74	1.61	-0.02	153.9	94.2	129.9	112.3	126.6	107.4	121.6	146.2	147.1	146.3	100.2	129.2	107.4	131.6	128.3	99.4	130.8	130.8
Fe I	4073.76	3.27	-0.90	22.5	13.4	15.4	13.4
Fe I	4076.63	3.21	-0.53	46.6	18.8	31.0	30.6	...	34.0	30.1	...	42.2	43.1	20.1	...	32.0	14.2	...	31.4
Fe I	4079.84	2.86	-1.36	22.2	13.4	21.1	...	15.8
Fe I	4109.06	3.29	-1.56	11.4	11.1	17.6x	8.9
Fe I	4109.80	2.85	-0.94	45.0	20.5	...	30.5	44.2	34.5	41.3	...	37.1	...	36.9	27.0	25.0
Fe I	4114.44	2.83	-1.30	31.1	18.8	24.9	23.0	24.0	21.3	14.8	6.2
Fe I	4127.61	2.86	-0.96	42.9	3...	35.1	37.2	35.5	25.6	12.0	...	22.7
Fe I	4132.90	2.85	-1.01	41.9	...	26.2	22.8	26.4	26.6	28.6	...	38.6	40.4	...	34.1	...	34.3	24.7	23.0
Fe I	4134.68	2.83	-0.65	62.3	...	38.1	40.9	27.5	37.8	43.1	60.3	57.8	45.4	24.8	55.8	21.6	44.2	43.2	20.6	47.9	40.1
Fe I	4137.00	3.41	-0.45	27.0	18.4	26.4	27.3	24.1	18.1	17.7
Fe I	4139.93	0.99	-3.63	33.7	13.7	...	12.1	28.9	15.0	9.3
Fe I	4143.87	1.56	-0.51	137.8	82.2	117.7	89.5	107.9	105.4	108.3	124.2	126.5	117.5	81.4	109.2	97.6	102.3	109.4	88.5	114.1	115.8
Fe I	4147.67	1.49	-2.10	80.1	25.7	52.9	37.9	5...	49.9	51.4	74.8	63.1	65.4	27.9	56.0	36.0	54.8	54.0	25.0	55.2	45.9
Fe I	4152.17	0.96	-3.23	59.3	...	30.1	19.6	...	27.8	32.0	51.7	41.8	47.8	...	44.8	15.5	32.2	29.8	24.0
Fe I	4153.90	3.40	-0.32	44.1	22.5	35.6	36.0	39.9	34.3	...	38.9	14.9	33.2	29.3	23.7
Fe I	4154.50	2.83	-0.69	56.3	...	36.6	39.1	46.3	50.1	53.7	...	39.3	...	12.6	...	29.2
Fe I	4156.80	2.83	-0.81	36.0	21.1	43.1	53.5	52.6	57.5	...	47.6	25.2	46.7	37.5	17.6
Fe I	4157.78	3.42	-0.40	38.3	22.5	30.7	39.2	29.3	32.4	...	34.5	14.0	28.2	29.0	...	21.5	17.9
Fe I	4158.79	3.43	-0.67	23.1	16.4	17.6	22.5	19.4	6.8	...	15.6	10.4
Fe I	4174.91	0.92	-2.97	78.6	...	43.0	30.4	49.7	...	50.3	...	48.4	62.0	15.8	62.7	29.4	60.6	...	18.7	39.6	39.0
Fe I	4175.64	2.85	-0.83	53.6	...	36.3	39.4	23.2	...	39.8	49.2	48.0	41.4	16.4	45.8	2...	45.6	41.0	16.1	32.1	33.7
Fe I	4181.75	2.83	-0.37	73.4	...	54.6	44.1	46.1	49.7	58.8	75.6	68.9	65.4	33.5	59.6	39.2	60.4	64.7	31.4	49.0	50.2
Fe I	4182.38	3.02	-1.18	25.3	16.4	16.0	...	25.0	...	14.2	11.2
Fe I	4184.89	2.83	-0.87	45.7	23.6	17.7	...	33.7	39.0	37.1	35.6	...	33.8	29.7	...	29.5	27.4

Table 3—Continued

Fe I	4187.04	2.45	-0.55	88.0	37.6	72.7	62.6	61.7	62.4	69.6	82.7	82.1	78.0	45.4	72.9	52.0	66.4	67.6	43.5	69.7	65.6
Fe I	4187.79	2.42	-0.55	94.8	50.7	75.7	64.5	65.3	61.6	75.2	83.9	84.3	84.2	47.1	81.0	55.5	78.4	80.5	50.5	73.7	73.9
Fe I	4191.43	2.47	-0.67	84.4	49.0	63.1	48.1	47.9	49.5	63.5	...	74.8	71.6	32.1	69.6	41.4	62.3	61.6	34.1	53.5	60.1
Fe I	4195.33	3.33	-0.49	44.2	31.2	38.4	39.2	34.4	39.3	...	41.9	...	37.5	38.5	9.0	...	23.8
Fe I	4196.21	3.40	-0.70	23.5	20.4	21.8	19.3	...	18.5	13.9	11.0	
Fe I	4199.10	3.05	0.16	80.6	46.3	65.1	60.8	56.1	58.9	65.5	79.5	79.0	79.4	45.7	78.6	47.9	65.3	72.1	39.2	63.9	63.0
Fe I	4216.18	0.00	-3.36	112.8	47.7	93.5	71.0	94.0	86.1	84.1	107.6	90.2	97.8	...	90.8	66.8	84.7	...	58.8	78.8	76.8
Fe I	4222.21	2.45	-0.97	72.0	29.5	51.4	40.2	54.7	45.0	52.9	69.2	62.5	59.7	...	61.3	42.5	54.5	48.1	27.7	43.9	51.0
Fe I	4227.43	3.33	0.27	93.4	34.3	71.5	56.2	52.8	65.4	65.5	99.4x	89.1	74.9	39.8	76.9	46.5	68.3	67.5	33.5	70.3	67.6
Fe I	4233.60	2.48	-0.60	83.8	33.2	67.4	49.0	61.2	59.8	65.1	86.1	75.9	73.9	38.5	75.5	51.7	68.8	61.0	41.4	61.3	64.9
Fe I	4238.81	3.40	-0.23	44.7	...	35.2	27.9	31.2	...	33.2	39.3	41.0	44.0	...	48.1	...	36.7	35.3	...	31.9	26.5
Fe I	4250.12	2.47	-0.41	94.5	51.7	76.2	61.1	63.7	74.6	76.4	81.4	90.5	90.2	52.0	77.5	56.9	79.4	74.2	46.1	67.5	72.9
Fe I	4250.79	1.56	-0.71	129.6	85.9	109.7	86.8	101.7	108.6	119.8	115.5	78.4	103.9	88.1	101.3	103.9	81.5	100.8	103.5
Fe I	4260.47	2.40	0.08	120.1	70.5	105.3	88.7	94.1	85.5	99.2	111.9	112.3	109.9	71.2	98.7	79.4	99.0	94.8	73.2	100.4	97.8
Fe I	4271.15	2.45	-0.35	103.6	57.5	83.0	80.8	76.7	98.8	89.4	95.8	89.7	91.1	54.7	105.1	64.1	92.8	99.6	54.3	73.2	79.9
Fe I	4282.40	2.18	-0.78	91.2	39.8	66.2	63.8	62.7	68.6	71.5	85.1	80.5	79.9	44.0	83.9	52.6	70.5	70.8	47.2	70.4	64.8
Fe I	4325.76	1.61	0.01	162.1	100.1	142.9	123.3	130.6	120.7	131.1	151.2	146.8	144.4	103.1	148.5	115.5	133.9	140.6	107.8	133.4	134.8
Fe I	4337.05	1.56	-1.70	61.8	...	62.2	75.5	...	74.1	74.6	...	75.0
Fe I	4352.73	2.22	-1.29	75.7	...	51.2	40.8	43.2	...	56.1	72.7	24.4	75.1	35.6	57.6	...	24.5	53.3	46.7
Fe I	4422.57	2.85	-1.11	46.5	...	30.3	...	18.6	...	31.8	...	36.2	35.7	...	37.6	13.9	29.3	25.2	29.8
Fe I	4427.31	0.05	-2.92	133.8	82.3	107.6	...	112.8	102.4	10...	...	112.8	114.1	68.8	99.8	80.2	91.8	...	78.0	88.8	95.3
Fe I	4430.61	2.22	-1.66	54.9	...	34.5	43.1	39.7	17.2	27.1	28.4
Fe I	4442.34	2.20	-1.25	77.5	28.3	56.4	48.5	44.3	50.5	61.0	76.4	67.9	75.5	34.1	68.8	36.5	61.0	58.2	30.5	50.4	52.8
Fe I	4443.19	2.86	-1.04	39.0	...	20.2	17.8	11.4	16.4	24.5	34.0	28.5	36.6	10.2	30.6	13.5	28.1	25.0	23.1
Fe I	4447.72	2.22	-1.34	74.8	...	51.0	33.9	47.8	41.2	51.5	64.2	59.5	59.9	23.8	57.2	34.3	50.2	50.4	18.6	44.1	46.0
Fe I	4454.38	2.83	-1.30	28.2	...	13.8	11.7	11.2	...	18.1	29.6	...	23.2	...	20.1	11.2	19.9	17.8	...	13.7	16.3
Fe I	4461.65	0.09	-3.21	118.6	61.2	86.8	62.7	95.2	85.4	83.6	114.3	93.9	93.6	56.7	87.5	68.9	88.4	89.4	63.1	76.2	83.7
Fe I	4466.55	2.83	-0.60	86.3	31.6	56.3	38.3	48.5	52.7	58.2	8...	62.8	65.8	24.6	63.2	35.0	58.8	54.6	27.3	42.8	47.8
Fe I	4469.38	3.65	-0.48	12.9	17.9	25.4
Fe I	4476.02	2.85	-0.82	68.8	...	39.3	33.5	35.3	40.9	50.9	56.9	57.8	62.0	23.5	52.0	...	48.4	47.1	...	44.3	40.9
Fe I	4484.22	3.60	-0.86	17.8	13.7	17.2	15.8	8.9
Fe I	4489.74	0.12	-3.97	89.1	...	52.2	30.4	59.0	50.2	47.3	85.1	...	64.6	16.6	55.7	32.6	56.7	48.2	20.1	41.0	40.2
Fe I	4494.56	2.20	-1.14	84.6	...	59.2	50.7	54.8	52.7	...	79.0	68.9	70.8	35.6	64.5	39.6	68.2	62.8	32.4	51.3	52.2
Fe I	4528.61	2.18	-0.82	102.9	...	81.7	64.8	74.8	85.2	80.5	100.1	93.0	91.4	50.4	91.6	55.9	82.0	85.0	50.3	74.1	76.0

Table 3—Continued

Fe I	4531.15	1.49	-2.15	84.8	...	55.0	40.8	54.4	47.1	55.4	76.4	60.9	66.3	20.6	63.6	32.6	56.3	55.4	23.7	47.8	48.3
Fe I	4592.65	1.56	-2.45	69.2	...	39.6	26.8	34.7	32.5	38.1	65.4	35.9	52.1	13.9	47.6	19.1	4...	42.0	14.9	35.3	...
Fe I	4602.94	1.49	-2.21	83.2	...	51.5	32.3	52.4	44.6	55.0	78.9	58.9	61.6	...	62.0	29.8	54.6	5...	24.1	43.2	45.6
Fe I	4632.91	1.61	-2.91	35.0	29.8	...	27.8	...	22.4	16.9
Fe I	4647.44	2.95	-1.35	26.1	9.2	18.2	21.2	...	16.5	...	19.5	...	16.3	11.9
Fe I	4707.27	3.24	-1.08	28.3	11.8	26.2	27.0	19.3	...	24.4	14.4
Fe I	4733.59	1.49	-2.99	40.2	18.5	...	20.4	35.8	23.6	26.5	...	22.0	8.5	17.4	16.6	12.4
Fe I	4736.77	3.21	-0.75	45.0	...	26.0	22.1	21.1	18.1	26.5	36.5	34.8	34.6	...	35.1	15.7	33.1	26.0	...	23.2	25.2
Fe I	4859.74	2.88	-0.76	60.3	39.5	47.1	42.8	50.3	49.5	60.9	...	57.0	...	43.8	36.4
Fe I	4871.32	2.87	-0.36	79.7	...	61.2	52.6	...	53.2	58.9	75.2	...	64.5	31.1	63.1	38.8	63.3	57.9	30.4	56.3	56.4
Fe I	4872.14	2.88	-0.57	68.2	25.9	47.3	33.7	42.0	43.8	51.7	59.9	...	62.7	21.6	51.0	29.5	46.0	45.0	20.7	46.1	41.0
Fe I	4890.75	2.88	-0.39	82.1	27.1	58.5	48.2	48.3	52.1	59.0	72.3	68.9	67.4	30.7	62.2	4...	61.3	53.1	29.5	53.3	54.9
Fe I	4891.49	2.85	-0.11	95.4	51.7	70.7	65.9	62.6	70.5	67.8	85.9	84.4	75.7	43.5	74.2	51.6	70.5	68.2	45.2	65.8	68.6
Fe I	4903.31	2.88	-0.93	51.2	...	32.8	23.2	20.4	29.3	37.8	46.9	46.4	44.8	...	40.9	16.2	23.6	29.9	...	25.8	25.3
Fe I	4918.99	2.87	-0.34	82.1	34.0	64.8	53.7	55.5	56.8	61.5	76.1	79.5	69.3	31.1	69.1	42.2	61.7	58.0	34.5	61.9	55.2
Fe I	4920.50	2.83	0.07	106.0	57.9	85.2	75.7	77.4	79.4	85.0	96.9	91.5	89.9	54.3	97.5	61.1	80.2	84.8	57.2	83.4	78.4
Fe I	4924.77	2.28	-2.26	31.3	...	10.9	11.7	...	13.9	15.6	21.1	...	19.3	...	18.9	7.4	15.2	13.3	...	13.6	13.2
Fe I	4938.81	2.88	-1.08	42.8	...	29.6	16.8	24.0	20.9	29.0	34.2	37.3	26.5	13.1	35.0	14.4	27.7	20.9	11.8	25.2	21.4
Fe I	4939.69	0.86	-3.34	71.2	...	37.0	25.0	37.0	37.6	37.0	61.7	...	52.2	11.7	48.0	21.2	40.4	38.9	15.1	26.7	26.6
Fe I	4946.39	3.37	-1.17	16.1	15.4	13.7	14.2	6.9
Fe I	4966.09	3.33	-0.87	31.5	16.8	19.1	26.0	...	22.3	...	21.4	9.1	16.9	17.1	...	16.0	...
Fe I	4973.10	3.96	-0.95	7.7
Fe I	4994.13	0.92	-2.96	81.8	...	48.1	3...	43.5	40.5	46.0	75.5	51.6	61.1	...	48.2	25.5	45.6	47.3	20.3	36.5	37.1
Fe I	5001.87	3.88	0.05	32.2	...	2...	15.3	13.5	19.9	26.1	25.2	...	21.3	9.1	27.4	...	21.8	23.0	...	18.5	18.2
Fe I	5006.12	2.83	-0.61	71.8	23.8	47.8	40.5	38.6	42.6	49.8	68.0	68.1	57.7	24.0	56.5	28.0	55.1	47.7	17.7	49.0	...
Fe I	5012.07	0.86	-2.64	110.6	41.6	80.7	58.3	85.4	67.8	75.5	107.2	90.3	85.9	43.0	75.4	55.7	76.0	74.8	43.3	67.0	68.9
Fe I	5014.94	3.94	-0.30	25.2	13.8	15.1	18.8	23.8	14.9	...	22.1	15.5	...	9.0	...
Fe I	5022.24	3.98	-0.53	14.0
Fe I	5041.07	0.96	-3.09	87.4	...	50.5	26.5	47.5	46.7	52.4	84.1	53.2	60.4	15.6	57.4	26.5	52.8	...	17.6	39.7	44.1
Fe I	5041.76	1.49	-2.20	95.4	...	6...	45.7	55.1	50.3	61.3	90.3	71.2	74.7	26.0	68.5	33.1	64.8	...	22.3	54.2	54.5
Fe I	5044.21	2.85	-2.04	9.3	1...
Fe I	5049.82	2.28	-1.34	75.0	29.5	49.0	...	43.2	45.6	50.8	65.2	58.5	62.5	21.0	54.5	28.3	45.2	45.3	...	40.1	40.5
Fe I	5051.63	0.92	-2.80	100.6	33.0	68.2	45.0	64.8	64.2	64.0	93.6	71.3	80.2	28.2	65.4	40.1	65.6	63.5	31.5	54.0	57.5
Fe I	5068.77	2.94	-1.04	40.2	...	17.4	...	16.6	22.0	26.9	31.5	...	28.3	...	26.9	12.0	28.0	23.4	...	18.1	19.1

Table 3—Continued

Fe I	5074.75	4.22	-0.20	17.3	13.8	16.4
Fe I	5079.22	2.20	-2.07	43.2	15.5	15.0	23.5	39.1	26.4	...	27.8
Fe I	5079.74	0.99	-3.22	70.5	...	34.2	...	33.0	29.5	36.7	...	41.5	52.8	...	43.4	17.0	39.3	36.9	...	28.1
Fe I	5083.34	0.96	-2.96	55.2	...	52.0	54.2	5...	81.2	61.4	65.0	19.0	59.0	26.2	49.8	51.6	21.4	41.7
Fe I	5090.77	4.26	-0.36	6.7	5.1
Fe I	5098.70	2.18	-2.03	56.6	...	24.9	...	20.6	...	30.5	5...	40.6	37.8	...	39.5	14.6	30.7	27.1	...	25.3
Fe I	5110.41	0.00	-3.76	115.6	37.5	79.0	52.7	85.1	78.5	71.5	105.4	83.3	91.0	36.1	81.7	53.7	73.1	75.9	45.5	61.8
Fe I	5123.72	1.01	-3.07	76.9	...	42.3	23.7	43.9	36.5	42.2	...	48.7	56.5	14.4	53.0	...	41.0	39.8	15.7	29.9
Fe I	5125.12	4.22	-0.14	17.6	15.0	...	15.9	16.0
Fe I	5127.36	0.92	-3.31	69.8	21.7	35.1	31.1	33.3	68.6	44.0	46.1	...	43.4	16.8	34.1	...	15.9	26.6
Fe I	5133.69	4.18	0.14	31.2	25.2	27.1	33.8	26.8	...	26.6	9.7	26.4	19.4	...	20.4
Fe I	5142.93	0.96	-3.08	82.9	...	42.8	21.2	43.1	36.5	42.1	75.4	54.6	58.0	11.7	54.0	21.9	48.3	41.6	...	37.8
Fe I	5150.84	0.99	-3.00	73.7	...	40.2	26.3	36.2	38.5	38.7	59.4	50.5	5...	14.4	45.5	20.2	38.7	40.2	...	32.0
Fe I	5151.91	1.01	-3.32	61.7	...	33.1	20.4	28.2	31.1	...	52.9	38.5	40.3	9.2	34.0	14.2	33.5	25.8	10.2	22.2
Fe I	5162.27	4.18	0.02	26.5	15.4	12.0	...	21.5	18.6	26.9	18.9	10.9	24.6	...	16.9	16.0	...	18.9
Fe I	5166.28	0.00	-4.20	91.9	20.9	5...	32.4	51.8	51.0	50.3	86.8	56.3	68.1	14.7	51.1	27.2	50.1	48.3	23.2	35.1
Fe I	5171.60	1.49	-1.79	107.5	37.9	84.3	63.7	79.1	82.6	72.4	108.1	93.1	85.8	46.8	77.7	59.8	78.9	...	51.2	72.2
Fe I	5191.46	3.04	-0.55	60.7	21.0	36.5	36.4	28.7	31.5	44.0	50.2	61.7	54.0	18.8	49.5	24.4	43.7	39.8	15.5	34.9
Fe I	5192.34	3.00	-0.42	70.2	28.8	50.4	43.2	37.5	52.4	51.6	62.2	64.5	61.9	23.5	54.2	29.6	53.3	45.4	18.2	44.4
Fe I	5194.94	1.56	-2.09	9...	28.1	63.5	50.3	57.2	53.6	56.0	88.6	74.4	74.4	28.2	66.0	38.4	63.2	58.2	25.3	52.2
Fe I	5198.71	2.22	-2.13	37.7	12.3	20.5	30.1	25.9	24.1	34.5	...	13.0
Fe I	5202.34	2.18	-1.84	59.3	26.0	...	23.4	...	47.3	44.4	42.1	...	40.2	...	34.2	3...	...	26.9
Fe I	5216.27	1.61	-2.15	171.9x...	...	53.6	...	46.3	50.5	...	80.5	66.3	71.3	20.5	54.6	...	55.4	52.1	25.9	53.1
Fe I	5217.39	3.21	-1.07	10.1	...	20.4	19.9	21.4	...	11.8	...	15.1	12.9	...	11.4
Fe I	5225.52	0.11	-4.79	23.0	38.7	12.6	17.8	...	19.5	15.6	...	11.3
Fe I	5232.94	2.94	-0.06	71.3	...	62.3	63.5	...	82.9	83.0	78.6	...	74.9	...	69.4	70.9	42.9	64.2
Fe I	5242.49	3.63	-0.97	9.3	8.1
Fe I	5247.05	0.09	-4.95	14.7	34.3	...	16.0	13.7
Co I	3842.05	0.92	-0.77	56.7	23.0	34.7	32.4	39.1	27.3	32.4	54.7	40.4	45.8	24.0	40.3	21.5	34.8	35.4	23.3	49.3
Co I	3845.47	0.92	0.01	93.6	48.9	76.8	60.7	65.0	59.7	64.4	86.9	80.4	70.8	52.8	71.0	51.9	69.9	74.9	51.1	85.2
Co I	3881.87	0.58	-1.13	78.0	...	44.1	34.5	40.5	54.7	41.3	75.8	60.4	55.8	29.5	49.9	28.7	52.2	51.8	29.8	52.0
Co I	3995.31	0.92	-0.22	82.7	...	54.4	48.1	54.4	55.1	58.6	...	72.4	75.0	44.2	66.5	45.3	63.8	68.2	41.1	71.6
Co I	4020.90	0.43	-2.07	40.6	...	12.8	34.2	20.2	26.8	11.2	20.4	14.0	7.8	1...
Co I	4110.53	1.05	-1.08	39.8	...	17.5	13.9	30.8	17.0	34.3	...	24.0	15.1	16.9	16.2	...	20.7

Table 3—Continued

Co I	4118.77	1.05	-0.49	84.9	51.1	52.1	49.2	77.2	68.8	34.5	6...	55.7	30.6	66.2	...
Co I	4121.32	0.92	-0.32	90.3	50.4	70.6	55.3	69.8	67.6	60.6	90.9	79.2	77.6	41.9	71.4	48.8	67.3	70.2	46.7	71.3	61.1
Ni I	3807.14	0.42	-1.22	115.4	78.2	97.8	81.2	89.0	9...	84.4	107.4	107.9	99.3	70.2	88.2	78.7	89.3	94.8	74.4	...	93.3
Ni I	3858.30	0.42	-0.95	126.6	87.9	106.4	91.2	104.6	87.3	90.2	114.3	117.4	100.6	79.8	91.4	83.5	94.3	102.2	79.2	113.8	99.5
Ni I	4648.66	3.42	-0.16	17.1	7.3	10.3	16.0	16.0	...	8.2	7.6
Ni I	4714.42	3.38	0.23	31.5	...	15.7	17.1	15.6	...	18.4	21.8	26.6	23.3	...	23.3	8.8	16.5	18.9	...	32.7	19.9
Ni I	4855.41	3.54	0.00	17.8	...	6.9	10.7	9.7
Ni I	4980.16	3.61	-0.11	16.1	8.9	9.0	12.2	14.2	7.3
Ni I	5035.37	3.63	0.29	21.4	16.3	13.0	12.2	10.3
Ni I	5080.52	3.65	0.13	22.5	10.1	14.2	...	13.5	13.7
Ni I	5137.08	1.68	-1.99	36.2	14.9	14.1	28.0	...	20.9	15.9	11.2	...	22.4	...
Zn I	4722.15	4.03	-0.39	14.9	...	14.7	...	5.0	11.3	8.2	11.2	15.1	13.0	...	13.3	6.0	10.1	9.6	4.9	7.5	1...
Zn I	4810.53	4.08	-0.17	22.8	...	14.1	13.6	...	16.4	10.4	11.8
Sc II	4246.82	0.31	0.24	133.6	77.0	115.3	79.2	106.1	115.7	97.3	157.8	129.2	112.6	79.9	107.9	86.9	105.0	105.3	92.3	107.2	113.0
Sc II	4320.75	0.61	-0.25	102.7	34.0	...	51.3	72.8	58.8	63.3	122.9	102.3	71.1	37.7	77.2	50.4	75.2	74.8	49.6	73.2	81.9
Sc II	4325.00	0.60	-0.44	100.8	28.5	69.8	43.2	60.7	66.1	58.1	110.8	77.8	81.2	32.5	...	42.7	...	85.6	45.7	59.0	62.7
Sc II	4415.54	0.60	-0.67	72.2	22.5	41.0	...	66.6	53.2	...	46.2	43.3	55.2
Sc II	5031.01	1.36	-0.40	42.1	...	21.5	21.4	17.8	64.7	31.8	28.5	...	26.5	10.1	20.1	20.1	13.7	...	26.0
Ti II	3813.39	0.61	-2.02	97.0	...	80.2	47.4	55.5	...	62.1	...	90.5	75.8	34.7	68.5	49.4	66.4	74.0	46.8	64.2	73.6
Ti II	3882.29	1.12	-1.71	41.3	...	29.1	...	31.8	79.3	71.3	36.8	20.8	...	38.3	40.2
Ti II	4012.40	0.57	-1.75	104.8	...	90.8	63.3	67.7	82.2	73.5	113.5	109.1	103.3	41.8	...	68.1	82.9	...	52.1	73.9	87.3
Ti II	4025.12	0.61	-1.98	86.1	...	74.6	44.7	50.6	60.1	48.4	98.5	77.7	51.6	24.8	62.4	38.8	57.7	61.5	33.9	59.1	60.5
Ti II	4028.35	1.89	-1.00	55.4	...	41.9	...	23.1	43.1	34.0	68.6	66.3	44.6	...	49.8	23.3	36.7	44.3	12.2	27.9	41.2
Ti II	4053.83	1.89	-1.21	41.9	...	33.7	18.9	...	28.3	...	55.8	46.6	41.2	...	34.4	14.1	29.1	25.7	...	25.9	32.5
Ti II	4161.53	1.08	-2.16	54.5	20.2	22.4	27.7	69.4	47.5	49.0	...	31.0	13.8	33.4	31.5	11.7	31.0	32.2
Ti II	4163.63	2.59	-0.40	44.8	24.5	17.5	32.2	31.0	56.2	49.8	39.7	23.3	35.6	33.3	...	31.3	40.9
Ti II	4184.31	1.08	-2.51	30.9	22.4	41.7	34.2	8.8	...	23.3	14.8
Ti II	4287.88	1.08	-2.02	72.0	...	56.1	42.7	41.8	86.9	71.8	61.6	20.1	55.0	30.4	48.8	45.1	20.4	42.5	53.9
Ti II	4290.22	1.16	-1.12	112.8	55.2	99.6	74.7	67.7	...	79.4	122.4	116.2	90.9	56.6	96.2	67.5	92.1	93.0	60.3	87.3	95.0
Ti II	4330.72	1.18	-2.06	35.3	26.0	...	69.6	...	31.3	31.4	...	24.2	...
Ti II	4337.88	1.08	-1.13	56.7	...	72.2	75.5	110.6	107.1	85.9	52.4	97.4	87.1
Ti II	4344.30	1.08	-2.09	66.6	82.7	65.8	54.0	20.5	...	44.7	...	41.5	...
Ti II	4417.71	1.16	-1.43	102.2	36.0	85.9	66.2	...	101.5	...	34.4	87.2	59.3	74.8	...	45.2	73.1	81.9
Ti II	4418.31	1.24	-1.99	55.7	...	46.0	...	27.2	...	23.7	...	47.8	33.8	13.9	44.7	18.6	33.8	...	13.1	24.2	33.3

Table 3—Continued

Ti II	4441.73	1.18	-2.41	39.8	...	26.0	...	15.1	20.9	13.9	56.0	38.4	33.2	...	25.4	...	22.4	21.2	9.8	22.9	22.5
Ti II	4443.77	1.08	-0.70	120.5	60.4	11...	75.1	86.1	96.5	90.4	132.8	125.4	109.3	67.1	10...	79.4	96.2	97.7	71.5	97.9	109.0
Ti II	4444.54	1.12	-2.21	32.2	14.3	15.2	24.1	19.6	63.4	47.7	37.3	...	31.5	13.6	27.9	27.1	8.5	26.0	30.5
Ti II	4450.50	1.08	-1.51	89.3	...	74.4	42.0	46.9	64.1	58.8	100.2	92.4	73.1	29.5	71.2	45.3	66.3	65.0	34.3	64.8	70.5
Ti II	4464.46	1.16	-2.08	68.4	...	50.8	26.6	33.0	41.8	36.8	81.2	67.3	59.4	13.1	49.2	26.3	40.1	41.6	18.6	40.5	47.3
Ti II	4468.52	1.13	-0.60	122.2	64.2	114.1	71.3	87.0	95.1	92.3	136.4	123.3	108.9	67.9	101.0	82.6	102.3	103.1	75.1	103.2	109.2
Ti II	4470.83	1.16	-2.28	17.5	59.8	...	33.3	...	32.1	14.0	24.0	30.8	...	24.6	...
Ti II	4501.27	1.12	-0.76	118.0	67.1	107.5	75.4	84.0	89.1	83.9	119.5	120.1	106.3	58.7	97.4	79.0	86.8	94.0	71.0	99.6	106.9
Ti II	4529.48	1.57	-2.03	44.3	19.6	23.5	56.6	46.9	30.3	13.8	31.6	12.4	25.5	27.0	...	23.6	26.9
Ti II	4563.77	1.22	-0.96	110.2	54.7	102.2	66.7	78.7	86.2	85.5	123.5	113.5	98.9	60.3	92.5	66.6	81.2	87.4	61.4	88.7	96.4
Ti II	4571.96	1.57	-0.53	111.5	...	98.9	71.7	72.6	84.2	84.0	124.7	118.0	99.7	56.0	90.8	68.3	79.9	93.0	61.3	90.6	98.1
Ti II	4589.92	1.24	-1.79	74.4	...	55.2	23.2	33.8	42.4	39.9	86.8	69.2	61.3	13.4	52.6	23.9	44.5	46.4	22.4	46.1	51.3
Ti II	4657.21	1.24	-2.32	37.5	15.9	15.3	51.1	21.5	...	15.3	19.0	20.3
Ti II	4708.65	1.24	-2.37	34.1	48.4	37.2	22.8	...	18.9	...	14.2	15.0	20.5
Ti II	4779.98	2.05	-1.37	33.2	...	22.7	13.7	17.3	44.6	...	28.9	...	24.2	8.8	17.5	18.5	6.4	18.4	18.9
Ti II	4798.51	1.08	-2.67	33.1	...	16.1	14.4	16.8	46.6	...	24.9	9.5	16.2	13.6
Ti II	4865.61	1.12	-2.81	25.8	13.5	32.9	22.5	17.2
Ti II	5129.15	1.89	-1.39	44.7	...	30.3	22.5	24.7	6...	45.2	26.4	...	30.7	14.8	24.5	25.3	...	19.4	30.1
Ti II	5185.90	1.89	-1.35	37.0	...	21.7	14.8	16.8	49.9	42.5	29.1	11.8	19.7	18.5	...	16.7	22.2
Ti II	5188.69	1.58	-1.21	92.1	...	70.7	45.7	41.8	60.3	57.3	102.0	96.4	...	21.9	71.1	37.8	63.2	62.8	3...	55.7	68.0
V II	3916.41	1.43	-1.05	34.6	8.5	45.6	33.6	23.3	15.4
V II	3951.96	1.48	-0.78	40.8	15.8	47.7	6.8	26.0	6.0	12.2	...	19.1
V II	4005.71	1.82	-0.52	32.4	...	21.0	...	11.0	...	12.7	42.4	33.0	25.5	4.2	18.0	...	24.2	19.0	10.5	26.6	23.9
V II	4023.38	1.80	-0.69	32.1	46.9	17.1	15.2	16.7	...	12.2
Fe II	4178.85	2.58	-2.48	57.9	...	50.8	21.3	40.8	34.3	37.6	45.4	61.4	44.6	17.1	44.5	20.6	39.8	41.5	15.9	46.8	43.6
Fe II	4233.17	2.58	-2.00	87.2	40.7	80.9	47.0	68.3	79.1	65.6	79.1	94.2	86.9	34.8	81.2	52.1	71.6	69.4	41.8	78.1	77.9
Fe II	4416.82	2.78	-2.60	50.7	17.7	27.1	...	50.2	43.9	...	29.3	32.3	29.4
Fe II	4491.40	2.86	-2.70	34.6	...	23.8	...	16.9	25.4	35.2	27.7	7.2	24.2	13.5	22.3	14.7	...	20.6	19.2
Fe II	4508.28	2.86	-2.58	51.6	...	44.0	17.6	25.8	33.9	30.7	44.5	58.8	43.7	11.0	42.0	19.8	34.7	31.4	17.7	40.7	37.1
Fe II	4515.34	2.84	-2.48	45.6	15.1	...	24.7	34.5	36.5	45.3	39.4	12.1	33.8	10.8	27.5	30.8	12.2	32.5	31.3
Fe II	4520.23	2.81	-2.60	43.7	...	34.7	15.4	21.6	21.4	24.7	32.7	43.5	31.8	...	26.7	13.8	23.2	21.2	8.3	33.5	30.2
Fe II	4522.63	2.84	-2.03	...	28.4	58.2	30.4	39.9	46.1	49.0	...	78.0	63.3	21.4	61.5	31.4	54.5	52.2	23.1	55.7	...
Fe II	4541.52	2.86	-3.05	22.4	14.3	17.1	29.6	21.2	...	14.3	13.2	11.9
Fe II	4555.89	2.83	-2.29	55.2	11.3	29.5	33.2	34.2	46.3	55.0	37.8	33.0	14.0	41.4	...

Table 3—Continued

Fe II	4576.33	2.84	-2.94	22.2	14.3	18.7	25.8	16.8	...	17.8	12.0
Fe II	4583.83	2.81	-2.02	84.2	29.7	70.3	48.4	56.7	57.7	62.9	74.1	83.9	72.3	34.9	65.3	44.6	66.5	61.8	33.5	69.6	69.3
Fe II	4620.51	2.83	-3.29	12.9	9.2	15.8	6.8
Fe II	4731.44	2.89	-3.36	17.7	10.9	10.6	18.2	9.2
Fe II	4923.93	2.89	-1.32	105.1	49.7	94.6	65.8	78.5	75.8	80.3	94.4	107.4	87.1	55.4	87.3	60.1	81.3	82.2	51.3	95.4	91.6
Fe II	4993.35	2.81	-3.67	7.2
Fe II	5018.45	2.89	-1.22	116.2	66.5	107.2	68.8	92.4	85.8	87.4	112.3	122.9	102.4	58.3	94.7	71.7	91.2	92.9	58.6	110.1	101.9
Fe II	5197.56	3.23	-2.10	38.6	...	27.7	16.9	17.8	17.9	25.7	31.2	42.4	33.7	10.7	28.5	12.3	26.0	21.6	...	27.4	24.4
Fe II	5234.62	3.22	-2.27	30.7	...	23.4	22.3	...	34.5	45.7	...	10.9	32.8	...	28.0	27.0	12.0	33.5	32.5
Sr II	4077.71	0.00	0.15	164.1	85.8	173.6	109.9	43.1	134.8	132.4	105.7	152.1	138.9	23.7	155.8	119.9	128.7	155.2	15.0	122.7	146.5
Sr II	4215.52	0.00	-0.18	156.0	77.6	155.8	114.4	31.6	131.9	122.2	...	146.0	133.5	19.9	138.0	113.7	114.3	143.5	...	105.6	136.4
Y II	3774.33	0.13	0.21	77.3	...	79.8	41.4	...	54.1	62.0	32.8	67.1	67.9	...	66.6	46.2	51.2	67.9	...	32.2	69.5
Y II	3788.69	0.10	-0.06	68.6	...	65.0	30.9	...	5...	48.9	23.0	53.3	56.5	...	63.7	39.9	44.6	60.6	...	25.7	60.6
Y II	3818.34	0.13	-0.98	31.6	...	28.2	17.2	...	20.4	19.2	...	29.3	17.1	8.3	24.1	22.9
Y II	3950.35	0.10	-0.49	48.5	...	53.6	29.2	35.1	11.4	40.2	33.1	...	47.5	23.6	30.4	43.7	...	17.5	40.5
Y II	4883.69	1.08	0.07	24.5	...	28.2	14.6	...	18.1	18.9
Y II	5087.43	1.08	-0.17	13.7	...	16.3	13.9	6.5	...	1...	7.5	...	11.5	11.8	9.0
Zr II	3836.76	0.56	-0.06	49.8	...	58.0	37.0	43.5	...	47.4	34.4	...	57.6	25.4	18.3	48.8	50.1
Zr II	4161.21	0.71	-0.72	24.9	...	32.3	16.7	16.6	...	21.7	19.5	...	23.4	7.1	13.8	25.6	21.6
Zr II	4208.99	0.71	-0.46	25.8	...	32.0	12.3x	...	21.8	24.7	26.4	...	30.8	10.9	14.3	21.3	18.2
Zr II	4317.32	0.71	-1.38	4.5	4.8	5.5
Ba II	4554.03	0.00	0.16	100.9	20.9	110.5	79.6	10.3	115.4	113.3	58.9	128.9	118.3	4.8	137.9	98.0	86.9	99.7	...	41.8	88.4
Ba II	4934.09	0.00	-0.16	92.0	13.2	101.6	71.3	10.5x	125.7	116.9	56.9	128.1	120.5	6.2x	140.2	87.4	75.8	95.0	...	30.1	72.6

^aThe ID's of the objects are given in Table 1. The symbol 'x' indicates the lines measured, but excluded from the abundance analysis.

Table 4. EQUIVALENT WIDTHS OF HEAVY ELEMENTS

	λ	χ	$\log gf$	$W(\text{m}\text{\AA})^a$										
	(\AA)		(eV)	1	3	4	6	7	9	10	12	13	14	15
La II	3949.10	0.40	0.49	19.9	23.7	...	37.5
La II	3988.52	0.40	0.21	20.4
La II	3995.75	0.17	-0.06	22.2
La II	4086.71	0.00	-0.07	6.1	16.1	11.0	12.8	...	26.4	7.0
La II	4123.23	0.32	0.13	7.6	15.3	13.3	20.2
La II	4333.74	0.17	-0.06	36.8
La II	4429.90	0.23	-0.35	20.8
Ce II	4083.23	0.70	0.24	7.4
Ce II	4222.60	0.12	-0.18	9.2
Ce II	4486.91	0.30	-0.36	9.2
Ce II	4562.37	0.48	0.33	6.8	7.7
Ce II	4628.16	0.52	0.26	4.3
Pr II	4062.80	0.42	0.66	8.2
Nd II	4021.34	0.32	-0.10	8.8	...	5.8	...	8.4
Nd II	4061.09	0.47	0.55	5.8	6.1	7.9	15.2	14.7	14.3	12.3	21.6	4.9	...	8.7
Nd II	4069.27	0.06	-0.57	6.3
Nd II	4109.46	0.32	0.35	14.8	10.5	16.7	28.5	8.5
Nd II	4446.39	0.20	-0.35	8.1
Nd II	4462.99	0.56	-0.04	9.0
Sm II	4519.63	0.54	-0.43	5.6
Sm II	4577.69	0.25	-0.77	3.5
Eu II	3819.67	0.00	0.51	17.5	23.0	22.5	44.5	45.0	38.5	56.5	77.3	27.3	18.8	24.4
Eu II	4129.72	0.00	0.22	8.7	12.2	17.0	22.0	26.5	25.5	23.1	55.6	16.0	...	8.7
Eu II	4205.04	0.00	0.21	17.4	11.5	...	36.2	29.4	24.2
Gd II	3768.40	0.08	0.25	14.9	9.4	...	21.3
Gd II	3796.39	0.03	0.03	30.5
Gd II	3844.58	0.14	-0.51	6.1	8.7
Dy II	3869.86	0.00	-0.94	6.8
Dy II	3996.69	0.59	-0.19	7.1
Dy II	4103.31	0.10	-0.37	15.9	...	20.5	11.1
Er II	3692.65	0.05	0.13	7.2	29.5	25.5	...	30.4	31.8
Er II	3786.84	0.00	-0.64	77.7	74.4
Er II	3830.48	0.00	-0.36	8.4	18.3
Er II	3896.23	0.05	-0.24	14.9	...	13.9	...	24.1	32.7
Yb II	3694.19	0.00	-0.30	54.3	83.2

^aThe ID's of the objects are given in Table 1.

Table 5. ATMOSPHERIC PARAMETERS

Object	T_{eff}	$\log g$	[Fe/H]	v_{micro}
HD122563	4600	1.1	−2.5	2.2
BS 16033–008	5300	2.7	−2.8	1.6
BS 16080–054	4800	1.1	−3.0	2.4
BS 16083–172	5300	3.1	−2.5	1.5
BS 16084–160	4650	1.1	−3.0	2.2
BS 16089–013	4900	1.7	−2.7	1.9
BS 16543–097	5000	2.1	−2.7	1.6
BS 16934–002	4500	1.0	−2.8	2.0
BS 17439–065	5100	1.6	−2.5	2.3
CS 22886–042	4850	1.7	−2.5	1.9
CS 29516–041	5200	2.5	−3.0	1.7
CS 30306–132	5100	2.2	−2.5	1.9
CS 30312–059	4950	2.0	−3.0	1.8
CS 30319–020	5200	2.5	−2.5	1.7
CS 30325–028	4900	1.8	−2.8	2.0
CS 30325–094	5050	2.1	−3.0	2.0
CS 30327–038	5100	1.7	−2.7	2.2
CS 30329–004	5000	1.5	−2.7	2.2

Table 6. ABUNDANCE RESULTS

	Fe	Fe	C	Mg	Al	Si	Ca	Sc	Ti	Ti	Cr	Mn	Co	Ni	Zn	Sr	Y	Zr	Ba
HD 122563																			
$\log \epsilon(X)$	4.88	4.88	5.4	5.49	3.37	5.36	3.91	0.55	2.43	2.63	2.65	2.27	2.54	3.66	2.15	0.08	-0.84	-0.14	-1.69
$[X/Fe]([Fe/H])$	-2.62	-2.62	-0.4	0.53	-0.50	0.42	0.18	0.07	0.11	0.31	-0.42	-0.64	0.25	0.03	0.10	-0.22	-0.45	-0.13	-1.29
N	147	17		8	1	2	9	5	17	31	11	10	8	9	2	2	6	4	2
$\sigma([X/Fe])$	0.21	0.19		0.12	0.18	0.13	0.12	0.23	0.12	0.24	0.10	0.12	0.11	0.11	0.21	0.16	0.24	0.24	0.23
BS 16033-008																			
$\log \epsilon(X)$	4.66	4.64	6.2	5.06	2.69	...	3.68	0.41	2.28	2.43	2.27	1.79	2.53	3.72	< 2.21	-0.28	< -1.59	< -0.40	-1.86
$[X/Fe]([Fe/H])$	-2.84	-2.86	0.6	0.32	-0.96	...	0.17	0.15	0.18	0.33	-0.58	-0.90	0.46	0.31	< 0.38	-0.68	< -0.98	< -0.17	-1.24
N	58	7		5	1	...	5	4	2	6	3	3	3	2	...	2	1
$\sigma([X/Fe])$	0.20	0.19		0.11	0.17	...	0.11	0.23	0.11	0.24	0.10	0.10	0.15	0.10	...	0.24	0.21
BS 16080-054																			
$\log \epsilon(X)$	4.61	5.4	4.64	5.35	3.26	5.19	3.83	0.17	2.30	2.37	2.43	1.80	2.21	3.25	2.08	0.28	-0.72	0.12	-1.43
$[X/Fe]([Fe/H])$	-2.89	-2.87	-0.1	0.66	-0.34	0.52	0.37	-0.04	0.25	0.32	-0.37	-0.84	0.19	-0.11	0.30	0.25	-0.06	0.40	-0.76
N	114	11		8	2	2	8	3	10	26	6	4	7	4	2	2	6	3	2
$\sigma([X/Fe])$	0.20	0.18		0.10	0.17	0.12	0.10	0.23	0.11	0.24	0.11	0.14	0.12	0.10	0.21	0.15	0.24	0.24	0.23
BS 16083-172																			
$\log \epsilon(X)$	4.97	4.98	6.2	5.57	3.46	5.56	4.17	0.79	2.80	2.91	2.82	2.21	2.75	3.82	< 2.46	0.53	-0.40	< 0.483	-0.68
$[X/Fe]([Fe/H])$	-2.53	-2.52	0.34	0.52	-0.50	0.53	0.35	0.22	0.39	0.50	-0.34	-0.79	0.37	0.10	< 0.32	0.14	-0.10	< 0.40	-0.37
N	104	10		6	1	1	7	3	10	20	3	3	5	3	...	2	2	...	2
$\sigma([X/Fe])$	0.19	0.19		0.09	0.17	0.11	0.10	0.22	0.11	0.24	0.08	0.09	0.07	0.09	...	0.14	0.23	...	0.22
BS 16084-160																			
$\log \epsilon(X)$	4.40	4.40	5.2	4.80	3.03	5.09	3.47	0.00	1.80	1.92	2.07	1.43	2.01	3.07	< 1.79	-2.52	< -1.20	< -0.81	-3.23
$[X/Fe]([Fe/H])$	-3.10	-3.10	0.1	0.32	-0.36	0.63	0.22	0.00	-0.04	0.08	-0.52	-1.00	0.20	-0.08	< 0.22	-2.34	< -0.33	< -0.32	-2.35
N	113	12		7	2	2	7	3	7	20	6	3	6	3	...	2	1
$\sigma([X/Fe])$	0.21	0.20		0.13	0.19	0.15	0.13	0.24	0.14	0.25	0.12	0.13	0.12	0.13	...	0.25	0.22
BS 16089-013																			
$\log \epsilon(X)$	4.68	4.69	5.38	6.0	2.95	4.94	3.88	0.46	2.43	2.51	2.56	1.66	2.34	3.42	2.18	0.26	-0.77	0.08	-0.73
$[X/Fe]([Fe/H])$	-2.82	-2.81	0.4	0.62	-0.72	0.20	0.35	0.18	0.31	0.39	-0.31	-1.05	0.25	-0.01	0.33	0.16	-0.18	0.29	-0.13
N	107	12		7	1	1	9	4	11	24	6	3	6	4	1	2	4	3	2
$\sigma([X/Fe])$	0.22	0.20		0.14	0.19	0.15	0.14	0.25	0.14	0.25	0.13	0.13	0.16	0.17	0.23	0.25	0.25	0.27	0.24
BS 16543-097																			
$\log \epsilon(X)$	4.98	4.97	6.2	5.45	3.32	5.34	4.07	0.57	2.55	2.71	2.93	2.33	2.50	3.64	2.17	0.47	-0.50	0.37	-0.46
$[X/Fe]([Fe/H])$	-2.52	-2.53	0.3	0.39	-0.65	0.30	0.24	-0.01	0.13	0.29	-0.24	-0.68	0.11	-0.09	0.02	0.07	-0.21	0.28	-0.16
N	147	15		8	1	1	9	5	16	31	8	9	7	7	2	2	6	2	2
$\sigma([X/Fe])$	0.20	0.19		0.10	0.17	0.12	0.10	0.22	0.11	0.24	0.09	0.14	0.09	0.09	0.21	0.24	0.23	0.23	0.25
BS 16934-002																			
$\log \epsilon(X)$	4.71	4.69	5.3	6.04	3.73	5.01	3.93	1.01	2.63	2.85	2.72	2.01	2.41	3.37	1.92	-1.19	-1.93	< -0.21	-2.37
$[X/Fe]([Fe/H])$	-2.79	-2.81	-0.3	1.25	0.03	0.24	0.37	0.70	0.48	0.70	-0.18	-0.73	0.29	-0.09	0.04	-1.32	-1.37	< -0.03	-1.80
N	130	16		4	1	1	6	4	15	33	8	6	7	8	1	1	3	...	2
$\sigma([X/Fe])$	0.21	0.19		0.13	0.19	0.14	0.13	0.24	0.13	0.25	0.11	0.12	0.12	0.12	0.22	0.25	0.25	...	0.22
BS 17439-065																			
$\log \epsilon(X)$	5.11	5.13	5.5	5.73	3.23	5.43	4.21	0.79	2.84	2.99	2.92	2.43	2.78	3.87	2.34	0.26	-0.58	0.28	-0.63
$[X/Fe]([Fe/H])$	-2.39	-2.37	-0.5	0.54	-0.87	0.26	0.25	0.08	0.29	0.44	-0.38	-0.71	0.26	0.01	0.06	-0.27	-0.42	0.06	-0.46
N	129	18		7	1	1	7	5	12	30	5	5	8	4	2	2	6	3	2
$\sigma([X/Fe])$	0.20	0.18		0.10	0.17	0.12	0.10	0.23	0.11	0.24	0.09	0.19	0.11	0.10	0.21	0.23	0.08	0.08	0.21
CS 22886-042																			
$\log \epsilon(X)$	4.95	4.97	5.8	5.49	3.19	5.34	4.04	0.59	2.56	2.76	2.73	2.24	2.56	3.61	2.22	0.25	-0.70	0.10	-0.77
$[X/Fe]([Fe/H])$	-2.55	-2.53	0.0	0.46	-0.75	0.33	0.24	0.04	0.17	0.37	-0.41	-0.74	0.20	-0.09	0.10	-0.12	-0.38	0.04	-0.44
N	121	13		7	1	2	7	4	12	28	5	5	6	5	1	2	5	3	2
$\sigma([X/Fe])$	0.21	0.19		0.12	0.18	0.14	0.12	0.23	0.12	0.25	0.11	0.20	0.11	0.11	0.22	0.16	0.24	0.26	0.26
CS 29516-041																			
$\log \epsilon(X)$	4.53	4.51	5.5	5.11	3.05	5.27	3.58	0.30	2.21	2.32	2.24	1.54	2.40	3.28	< 2.11	-2.00	< -0.65	< -0.12	-2.75
$[X/Fe]([Fe/H])$	-2.97	-2.99	0.5	0.50	-0.47	0.68	0.20	0.17	0.24	0.35	-0.48	-1.02	0.46	0.00	< 0.41	-1.95	< 0.09	< 0.24	-2.00

Table 6—Continued

N	90	11		7	2	1	6	3	5	17	4	3	5	2	...	2	1
$\sigma([X/Fe])$	0.19	0.18		0.09	0.17	0.12	0.09	0.22	0.10	0.24	0.08	0.09	0.08	0.09	...	0.23	0.20
CS 30306–132																			
$\log \epsilon(X)$	5.10	5.08	6.5	5.66	3.56	5.44	4.25	0.80	2.79	2.95	3.06	2.48	2.78	3.76	2.42	0.67	-0.20	0.62	0.00
$[X/Fe]([Fe/H])$	-2.40	-2.42	0.5	0.48	-0.53	0.28	0.30	0.10	0.25	0.41	-0.23	-0.65	0.27	-0.09	0.15	0.15	-0.03	0.41	0.18
N	144	17		8	1	1	6	4	15	32	9	6	7	6	1	2	5	4	2
$\sigma([X/Fe])$	0.21	0.19		0.12	0.18	0.13	0.12	0.23	0.12	0.24	0.10	0.17	0.11	0.17	0.21	0.16	0.24	0.24	0.26
CS 30312–059																			
$\log \epsilon(X)$	4.46	4.48	5.6	5.10	2.64	5.11	3.66	0.17	2.16	2.32	2.21	1.55	2.19	3.13	1.94	0.07	-0.79	-0.15	-1.13
$[X/Fe]([Fe/H])$	-3.04	-3.02	0.3	0.56	-0.81	0.59	0.35	0.11	0.26	0.42	-0.44	-0.94	0.32	-0.08	0.31	0.19	0.02	0.28	-0.31
N	111	11		8	1	2	9	4	11	30	4	4	8	3	1	2	4	3	2
$\sigma([X/Fe])$	0.20	0.19		0.10	0.17	0.12	0.10	0.22	0.10	0.24	0.08	0.18	0.10	0.09	0.20	0.23	0.23	0.25	0.20
CS 30319–020																			
$\log \epsilon(X)$	5.15	5.13	6.4	5.60	3.48	5.66	4.18	0.91	2.83	2.99	3.00	2.48	2.90	3.79	2.30	0.51	-0.42	0.27	-0.90
$[X/Fe]([Fe/H])$	-2.35	-2.37	0.4	0.37	-0.66	0.45	0.18	0.16	0.24	0.40	-0.34	-0.70	0.34	-0.11	-0.02	-0.06	-0.30	0.01	-0.77
N	135	13		8	1	2	8	4	15	30	7	6	8	6	2	2	4	3	2
$\sigma([X/Fe])$	0.21	0.19		0.12	0.18	0.13	0.12	0.23	0.12	0.24	0.10	0.15	0.11	0.11	0.21	0.16	0.24	0.26	0.23
CS 30325–028																			
$\log \epsilon(X)$	4.76	4.77	6.2	5.44	3.23	...	3.93	0.56	2.40	2.59	2.66	2.14	2.45	3.47	2.11	0.45	-0.54	0.25	-1.14
$[X/Fe]([Fe/H])$	-2.74	-2.73	0.6	0.60	-0.52	...	0.32	0.20	0.20	0.39	-0.29	-0.65	0.28	-0.04	0.18	0.27	-0.03	0.38	-0.62
N	132	16		5	1	...	6	4	14	31	8	8	8	6	1	2	5	3	2
$\sigma([X/Fe])$	0.20	0.19		0.11	0.18	...	0.11	0.25	0.12	0.24	0.10	0.17	0.10	0.11	0.21	0.15	0.24	0.26	0.23
CS 30325–094																			
$\log \epsilon(X)$	4.33	4.36	5.7	4.96	2.66	5.25	3.52	0.30	2.17	2.21	2.06	1.31	2.26	2.97	1.90	-2.60	< -0.82	< -0.43	< -2.71
$[X/Fe]([Fe/H])$	-3.17	-3.14	0.5	0.55	-0.66	0.86	0.34	0.37	0.40	0.44	-0.46	-1.05	0.52	-0.11	0.40	-2.35	< 0.12	< 0.13	< -1.76
N	101	11		8	1	2	9	4	9	21	5	3	8	2	1	1
$\sigma([X/Fe])$	0.20	0.19		0.11	0.18	0.13	0.11	0.23	0.12	0.24	0.10	0.11	0.11	0.11	0.21	0.24
CS 30327–038																			
$\log \epsilon(X)$	4.86	4.88	< 5.6	5.49	3.22	5.40	3.85	0.44	2.47	2.57	2.67	2.40	2.78	3.98	2.08	-0.36	-1.15	< -0.35	-1.92
$[X/Fe]([Fe/H])$	-2.64	-2.62	< -0.1	0.55	-0.63	0.48	0.14	-0.02	0.17	0.27	-0.38	-0.49	0.51	0.37	0.05	-0.64	-0.74	< -0.32	-1.50
N	113	14		8	2	1	8	4	8	29	6	4	7	4	1	2	3	...	2
$\sigma([X/Fe])$	0.20	0.18		0.10	0.17	0.12	0.10	0.23	0.11	0.24	0.09	0.14	0.09	0.10	0.21	0.15	0.24	...	0.21
CS 30329–004																			
$\log \epsilon(X)$	4.75	4.74	5.4	5.44	3.19	5.28	3.95	0.45	2.53	2.56	2.61	1.98	2.40	3.55	2.10	0.19	-0.63	0.19	-1.46
$[X/Fe]([Fe/H])$	-2.75	-2.76	-0.2	0.61	-0.55	0.47	0.35	0.10	0.34	0.37	-0.33	-0.80	0.24	0.05	0.18	0.02	-0.11	0.33	-0.93
N	134	13		8	2	2	8	5	11	31	7	5	6	6	2	2	6	4	2
$\sigma([X/Fe])$	0.19	0.18		0.09	0.17	0.12	0.09	0.22	0.10	0.24	0.08	0.15	0.13	0.13	0.20	0.14	0.23	0.26	0.20

Table 7. ABUNDANCE RESULTS FOR HEAVY NEUTRON-CAPTURE ELEMENTS

	La	Ce	Nd	Sm	Eu	Gd	Dy	Er	Yb
HD 122563									
$\log \epsilon(X)$	-2.37	...	-1.93	...	-2.64	-2.33	...
$[X/Fe]$	-0.52	...	-0.80	...	-0.57	-0.68	...
N	1	...	1	...	3	1	...
$\sigma([X/Fe])$	0.29	...	0.25	...	0.25	0.25	...
BS 16080-054									
$\log \epsilon(X)$	-1.74	...	-2.46
$[X/Fe]$	-0.34	...	-0.12
N	1	...	3
$\sigma([X/Fe])$	0.24	...	0.24
BS 16083-172									
$\log \epsilon(X)$	-0.60	...	-1.35
$[X/Fe]$	0.44	...	0.63
N	1	...	2
$\sigma([X/Fe])$	0.24	...	0.24
BS 16089-013									
$\log \epsilon(X)$	-1.47	...	-0.94	...	-1.81
$[X/Fe]$	0.31	...	0.39	...	0.46
N	1	...	2	...	3
$\sigma([X/Fe])$	0.30	...	0.26	...	0.26
BS 16543-097									
$\log \epsilon(X)$	-1.34	-0.81	-0.82	...	-1.60	-0.85	...	-1.06	...
$[X/Fe]$	-0.04	0.08	0.21	...	0.37	0.58	...	0.49	...
N	3	1	2	...	3	2	...	3	...
$\sigma([X/Fe])$	0.24	0.24	0.24	...	0.24	0.24	...	0.24	...
BS 17439-065									
$\log \epsilon(X)$	-1.33	...	-0.98	...	-1.75	-1.38	-0.75
$[X/Fe]$	0.26	...	-0.08	...	0.09	-0.08	0.47
N	3	...	3	...	3	1	1
$\sigma([X/Fe])$	0.24	...	0.24	...	0.24	0.18	0.19
CS 22886-042									
$\log \epsilon(X)$	-1.43	...	-1.09	...	-1.86
$[X/Fe]$	0.28	...	-0.03	...	0.14
N	1	...	2	...	2
$\sigma([X/Fe])$	0.25	...	0.25	...	0.25
CS 30306-132									
$\log \epsilon(X)$	-0.76	-0.44	-0.45	-0.57	-1.14	-0.50	-0.48	-0.61	-0.77
$[X/Fe]$	0.42	...	0.46	...	0.71
N	7	5	6	2	2	3	3	3	1
$\sigma([X/Fe])$	0.25	0.25	0.25	0.25	0.25	0.25	0.25	0.25	...
CS 30312-059									
$\log \epsilon(X)$	-1.45	...	-1.95
$[X/Fe]$	0.10	...	0.54

Table 7—Continued

N	1	...	2
$\sigma([X/Fe])$	0.24	...	0.24
CS 30319–020									
$\log \epsilon(X)$	–1.76
$[X/Fe]$	0.04
N	1
$\sigma([X/Fe])$	0.26
CS 30325–028									
$\log \epsilon(X)$	–1.86	...	–1.29	...	–2.21	...	–1.02
$[X/Fe]$	–0.31	...	–0.04	...	–0.02	...	–0.02
N	1	...	2	...	2	...	2
$\sigma([X/Fe])$	0.29	...	0.25	...	0.25	...	0.25

Table 8. ERRORS FROM UNCERTAINTIES OF STELLAR PARAMETERS

Species	HD 122563		
	ΔT_{eff}	$\Delta \log g$	Δv_{tur}
	+100 K	+0.5 dex	+0.3 km s ⁻¹
[Fe/H](Fe I)	+0.13	-0.07	-0.10
[Fe/H](Fe II)	0.00	+0.15	-0.06
[Mg/Fe](Mg I)	-0.01	-0.06	+0.03
[Al/Fe](Al I)	+0.03	-0.08	-0.12
[Si/Fe](Si I)	-0.01	-0.09	-0.03
[Ca/Fe](Ca I)	-0.04	+0.00	+0.05
[Sc/Fe](Sc II)	-0.06	+0.19	-0.03
[Ti/Fe](Ti I)	+0.01	+0.02	+0.06
[Ti/Fe](Ti II)	-0.08	+0.20	+0.01
[Cr/Fe](Cr I)	+0.01	+0.01	+0.02
[Mn/Fe](Mn I)	0.00	+0.02	+0.04
[Co/Fe](Co I)	+0.03	+0.00	-0.01
[Ni/Fe](Ni I)	-0.02	+0.03	+0.03
[Zn/Fe](Zn I)	-0.10	+0.14	+0.08
[Sr/Fe](Sr II)	+0.02	+0.12	-0.20
[Y/Fe](Y II)	-0.06	+0.21	+0.04
[Zr/Fe](Zr II)	-0.06	+0.23	+0.08
[Ba/Fe](Ba II)	-0.04	+0.20	+0.04
Species	CS 30306-132		
	ΔT_{eff}	$\Delta \log g$	Δv_{tur}
	+100 K	+0.5 dex	+0.3 km s ⁻¹
[Sr/Fe](Sr II)	0.00	+0.03	-0.11
[Y/Fe](Y II)	-0.04	+0.21	+0.01
[Zr/Fe](Zr II)	-0.05	+0.21	+0.05
[Ba/Fe](Ba II)	-0.01	+0.21	-0.12
[La/Fe](La II)	-0.04	+0.22	+0.06
[Ce/Fe](Ce II)	-0.03	+0.21	+0.08
[Nd/Fe](Nd II)	-0.03	+0.21	+0.07
[Sm/Fe](Sm II)	-0.04	+0.21	+0.08
[Eu/Fe](Eu II)	-0.03	+0.22	+0.07
[Gd/Fe](Gd II)	-0.04	+0.22	+0.07
[Dy/Fe](Dy II)	-0.04	+0.22	+0.07
[Er/Fe](Er II)	-0.03	+0.22	+0.08
Species	CS 29516-041		
	ΔT_{eff}	$\Delta \log g$	Δv_{tur}
	+100 K	+0.5 dex	+0.3 km s ⁻¹
[Sr/Fe](Sr II)	-0.03	+0.21	+0.06
[Ba/Fe](Ba II)	-0.03	+0.22	+0.08

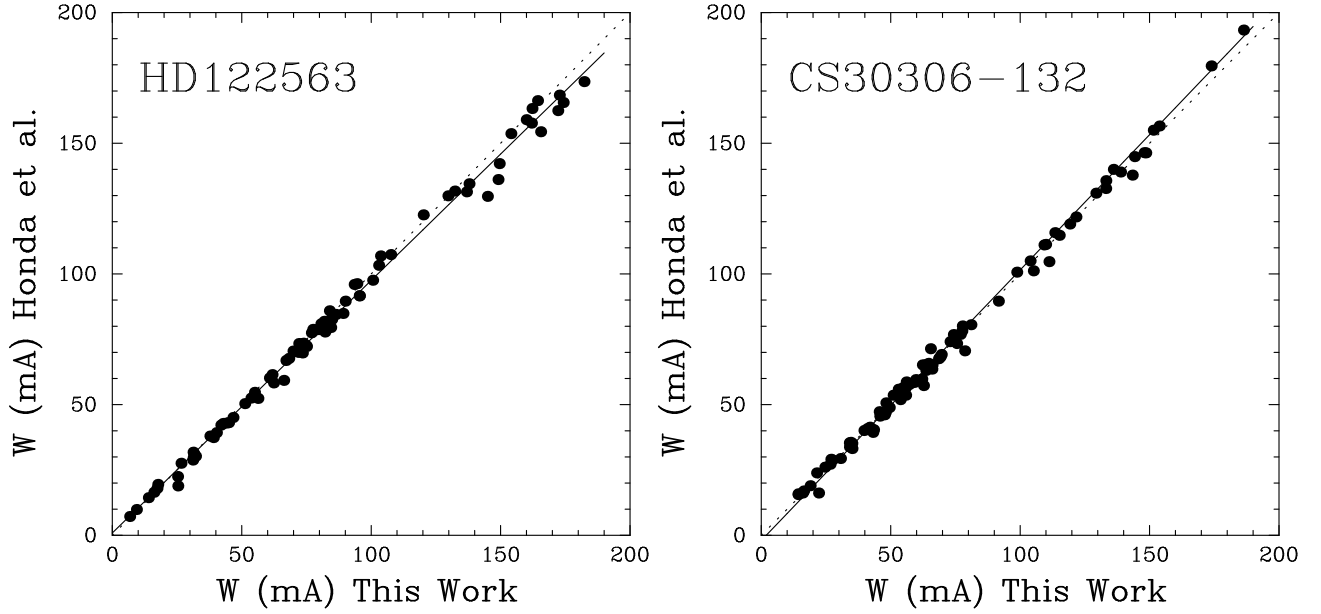


Fig. 1.— Comparisons of the equivalent widths of Fe I lines measured by Paper I and by the present work for HD 122563 and CS 30306–132. The solid line indicates the result of a least square fit, while the dotted line shows a line with a slope of unity.

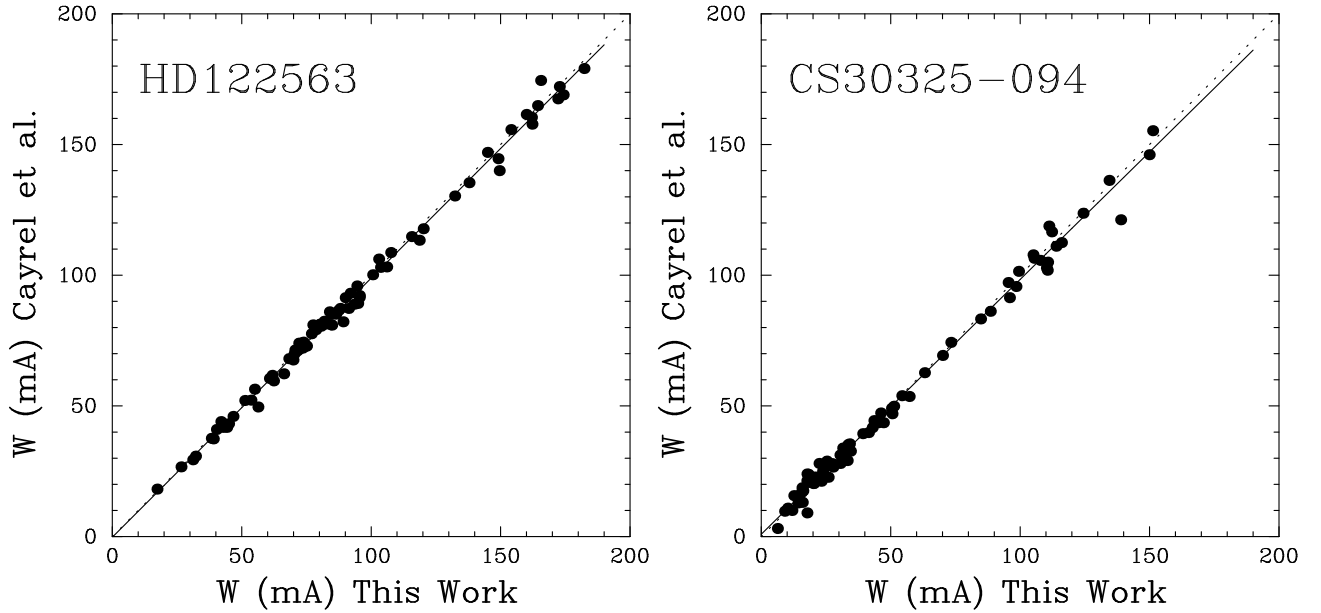


Fig. 2.— Comparisons of the equivalent widths of Fe I measured by Cayrel et al. (2004) and by the present work for HD 122563 and CS 30325–094. The meanings of the lines are the same as those in Figure 1.

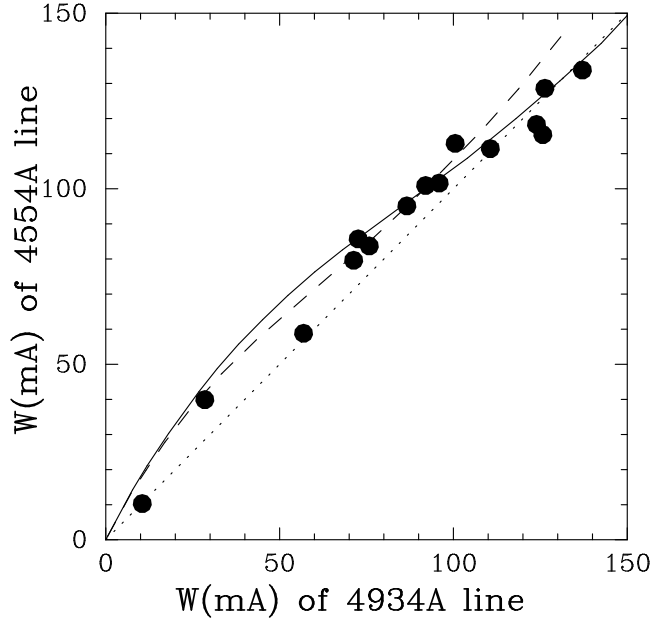


Fig. 3.— Comparisons of the equivalent widths of Ba II 4554 Å and 4934 Å lines (dots). The solid line indicates the comparisons of calculated equivalent widths including hyperfine splitting for the model atmosphere with $T_{\text{eff}} = 4900$ K, $\log g = 1.7$, and $[\text{Fe}/\text{H}] = -2.8$, assuming $v_{\text{turb}} = 1.9$ km s $^{-1}$. The dashed line shows the same comparison, but for the calculations not including hyperfine splitting. In the range of weak lines ($W \lesssim 50$ mÅ), the 4554 Å line is predicted to be stronger than the 4934 Å line. The difference becomes smaller in the stronger lines due to saturation effects. In the range of strongest lines ($W \gtrsim 120$ mÅ), the calculations including hyperfine splitting predict almost equal values of equivalent widths for both lines, while the calculations not including hyperfine splitting predict larger equivalent widths for the 4554 Å line than for the other line. The behavior of measured equivalent widths for the strongest lines can be well explained by the calculations including hyperfine splitting.

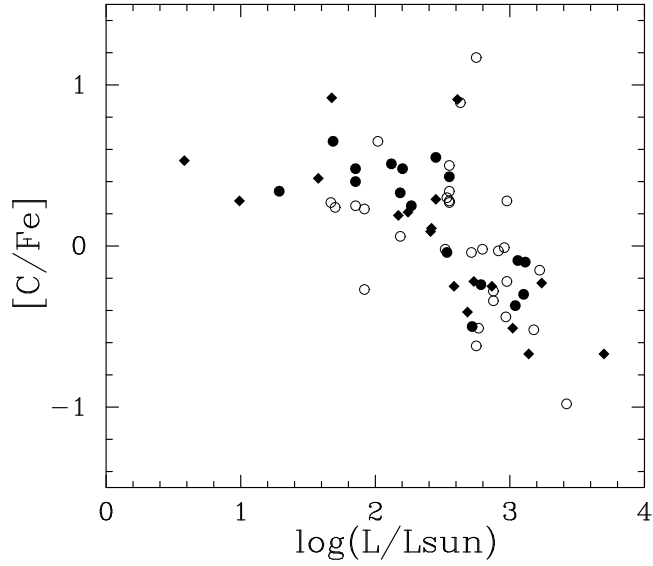


Fig. 4.— $[C/Fe]$ as a function of luminosity estimated from T_{eff} and $\log g$ (see text).

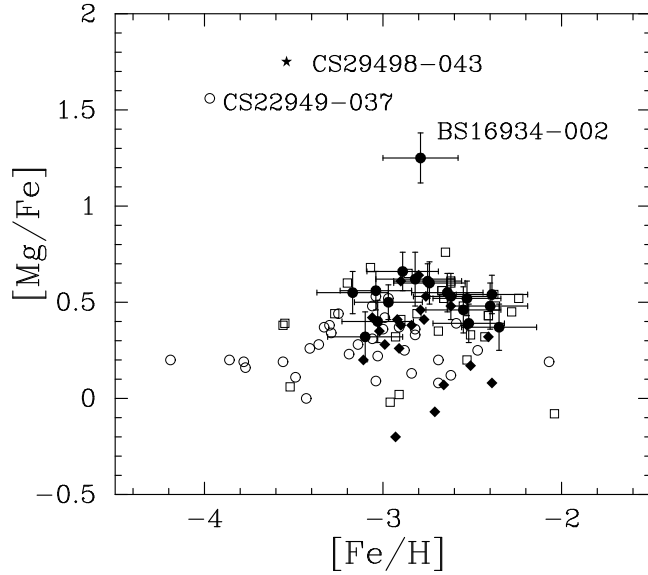


Fig. 5.— $[Mg/Fe]$ as a function of $[Fe/H]$. The results of the present study are shown by the filled circles with error bars. Results of previous studies are also shown by filled diamonds (Paper II), open circles (Cayrel et al. 2004; Depagne et al. 2002), open squares (Cohen et al. 2004; Carretta et al. 2002), and a filled star (Aoki et al. 2004). The three Mg enhanced stars (see text) are identified in the panel.

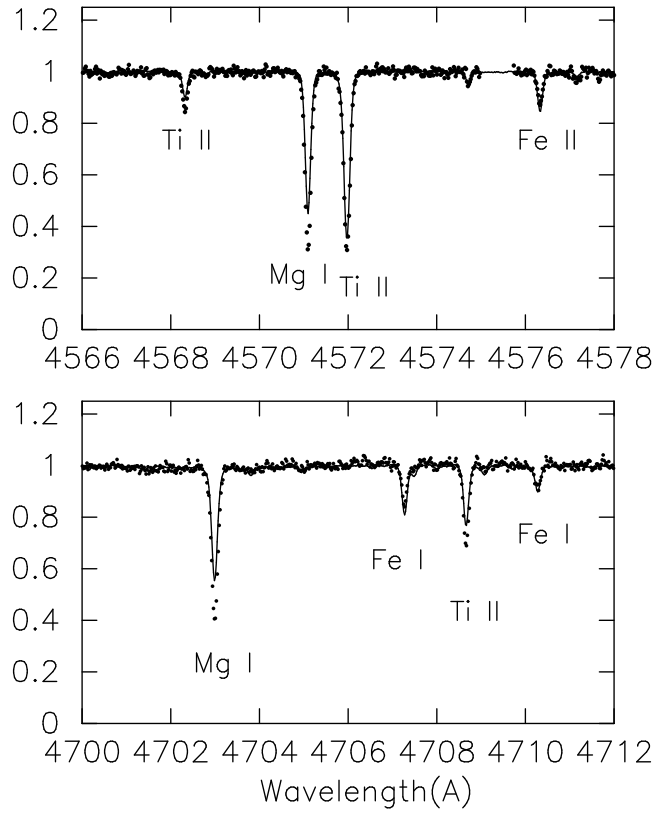


Fig. 6.— Comparisons of the spectrum of BS 16934–002 (filled circles) with that of HD 122563 (the line). These two stars have quite similar atmospheric parameters. The strengths of Fe I and Fe II lines are similar between the two stars, while the Mg I 4571 and 4703 Å lines of BS 16934–002 are much stronger than those of HD 122563. A small portion of the spectrum at around 4575 Å of BS 16934–002 was lost because of a defect of the detector.

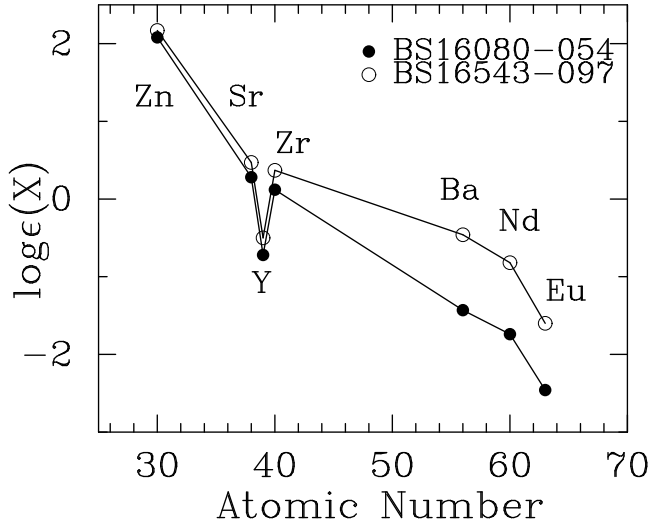


Fig. 7.— Elemental abundance patterns of BS 16080–054 (filled circles) and BS 16543–097 (open circles) from Zn to Eu. The abundances of heavy neutron-capture elements are significantly different between the two stars, while metallicity and abundances of light neutron-capture elements are quite similar.

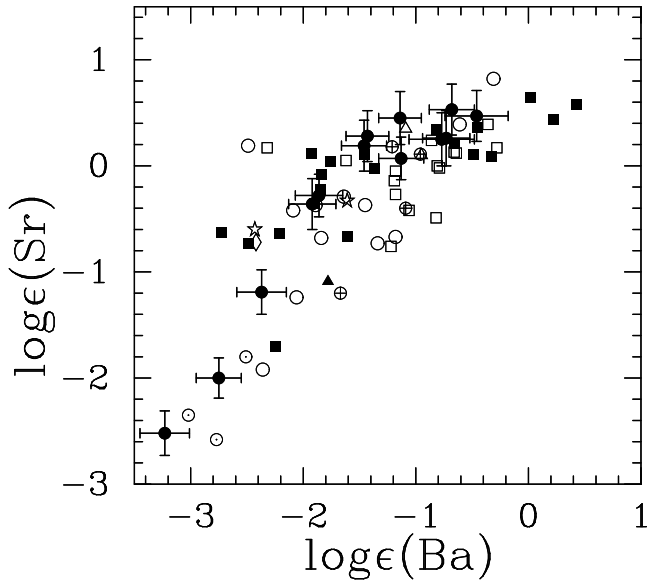


Fig. 8.— Sr abundances as a function of the Ba abundance for very metal-poor stars ($[\text{Fe}/\text{H}] \leq -2.5$). Stars having significant excesses of carbon and s-process elements are excluded. The present results are shown by filled circles with error bars. Results of previous studies are also shown by filled squares (Paper II), open circles (McWilliam et al. 1995; McWilliam 1998), open squares (Cohen et al. 2004; Carretta et al. 2002), circles with cross (Johnson & Bolte 2002), open triangles (Borris et al. 2000), open stars (Ishimaru et al. 2004), circles with enclosed point (Francqis et al. 2003), an open diamond (Depagne et al. 2002), and a filled triangle (Aoki et al. 2004).

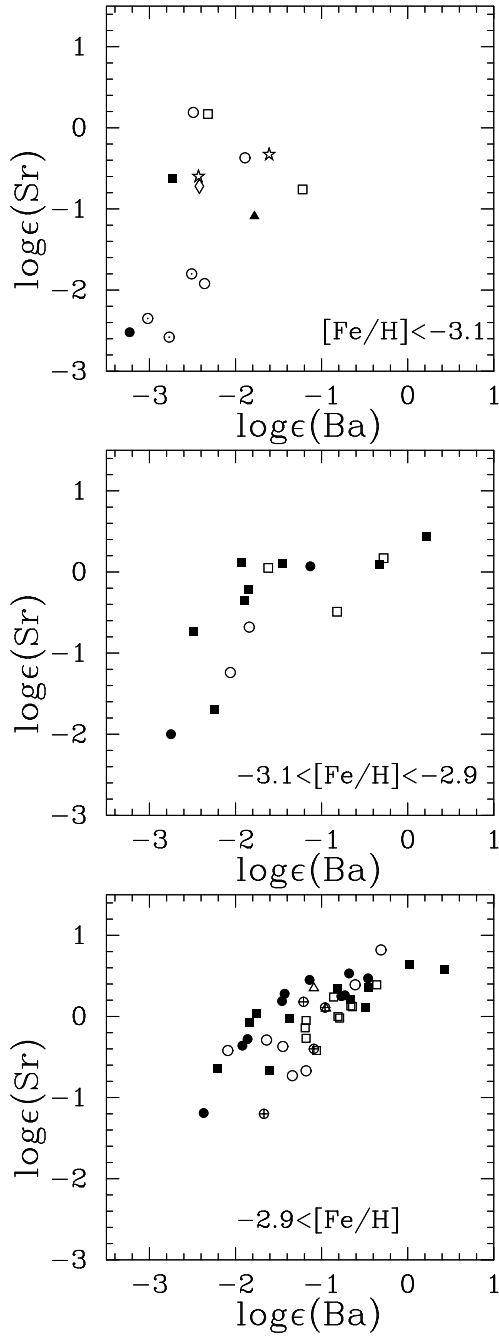


Fig. 9.— The same as Fig. 8, but for stars with $[\text{Fe}/\text{H}] \leq -3.1$ (top), $-3.1 < [\text{Fe}/\text{H}] \leq -2.9$ (middle), and $-2.9 < [\text{Fe}/\text{H}] \leq -2.5$ (bottom). The open diamond and the filled triangle in the top panel denote the abundances of CS 22949–037 and CS 29498–043, respectively, which have very low iron abundances but large enhancements of carbon and the α -elements.

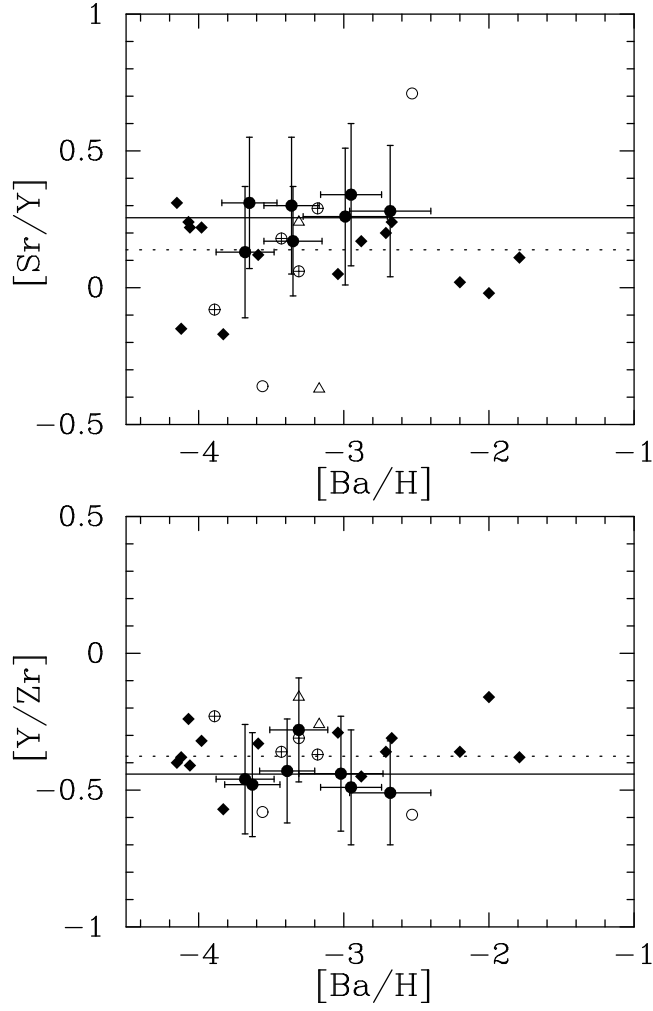


Fig. 10.— $[\text{Sr}/\text{Y}]$ (top) and $[\text{Y}/\text{Zr}]$ (bottom) as functions of $[\text{Ba}/\text{H}]$. The symbols have the same meanings as in Figure 8. The solid line shows the average value of $[\text{Sr}/\text{Y}]$ or $[\text{Y}/\text{Zr}]$ of 7 stars in our sample in which all of these three elements are detected. The dotted line indicates the average value of all stars shown in the figure (29 stars) including objects studied by previous work.

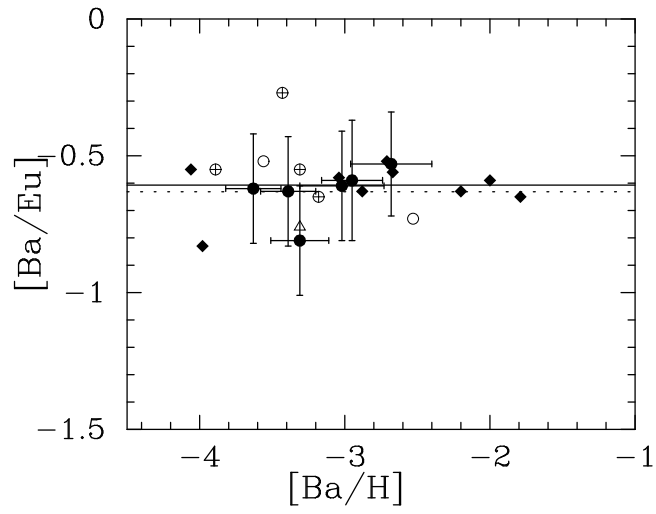


Fig. 11.— The same as Fig. 10, but for $[Ba/Eu]$

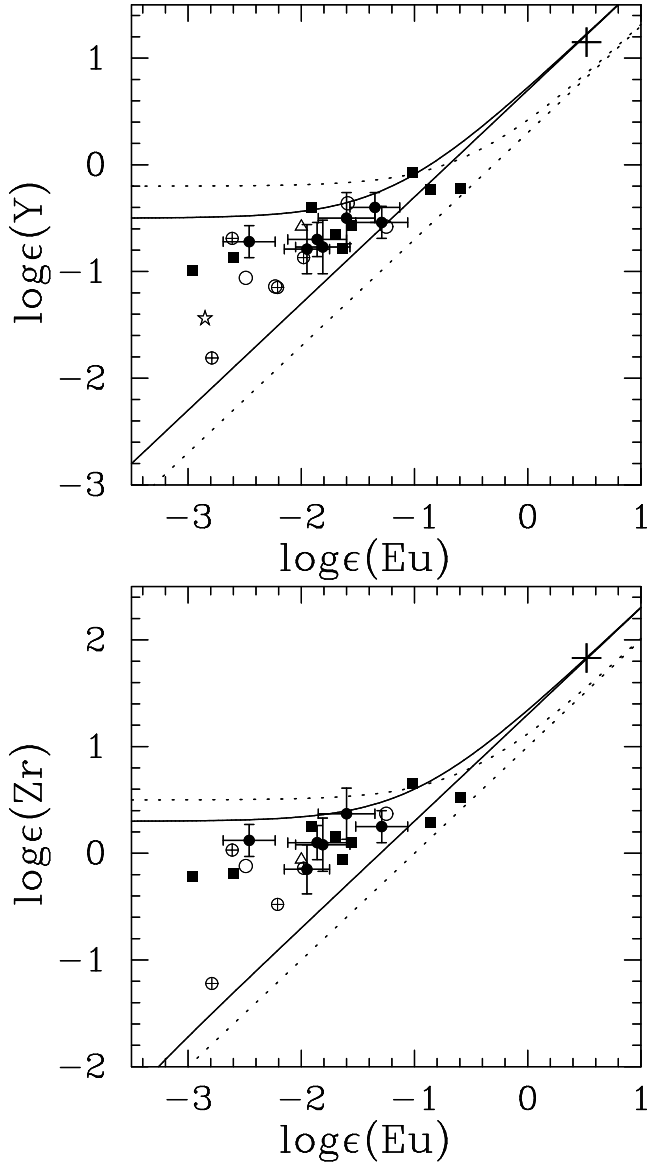


Fig. 12.— Abundances of Y and Zr as functions of the Eu abundance. The meaning of the symbols is the same as in Fig. 8. The solid and dotted lines show the enrichment of related elements assuming different initial abundances and a constant Y/Eu or Zr/Eu ratios in the yields of the main r-process. See text for details. The cross indicates the abundances of the r-process component of solar-system material estimated by Arlandini et al. (1999).